THE GEOLOGICAL SOCIETY OF AMERICA®

Pyrite-walled tube structures in a Mesoproterozoic sediment-hosted metal sulfide deposit

Theodore M. Present[1,†], Kristin D. Bergmann[2,§], Corinne Myers[2,#], Sarah P. Slotznick[1,††], Jessica R. Creveling[1,§§], Jerry Zieg[3], Woodward W. Fischer[1], Andrew H. Knoll[2], and John P. Grotzinger[1]

[1]*Division of Geological and Planetary Sciences, California Institute of Technology, MC 170-25, Pasadena, California 91125, USA*
[2]*Department of Organismic and Evolutionary Biology, Harvard University, Cambridge, Massachusetts 02138, USA*
[3]*Tintina Resources Inc., 17 E. Main Street, P.O. Box 431, White Sulphur Springs, Montana 59645, USA*

ABSTRACT

Unusual decimeter-scale structures occur in the sediment-hosted Black Butte Copper Mine Project deposit within lower Mesoproterozoic strata of the Belt Supergroup, Montana. These low domal and stratiform lenses are made up of millimeter-scale, hollow or mineral-filled tubes bounded by pyrite walls. X-ray micro–computed tomography (micro-CT) shows that the tube structures are similar to the porous fabric of modern diffuse hydrothermal vents, and they do not resemble textures associated with the mineralization of known microbial communities. We determined the sulfur isotopic composition of sulfide minerals with in situ secondary ion mass spectrometry (SIMS) and of texture-specific sulfate phases with multicollector–inductively coupled plasma–mass spectrometry (MC-ICP-MS). The sedimentological setting, ore paragenesis, sulfur isotope systematics, and porosity structure of these porous precipitates constrain the site of their formation to above the sediment-water interface where metalliferous hydrothermal fluids vented into the overlying water column. These data constrain the geochemistry of the Mesoproterozoic sediment-water interface and the site of deposition for copper-cobalt-silver mineralization. Metals in the hydrothermal fluids titrated sulfide in seawater to create tortuous fluid-flow conduits. Pyrite that precipitated at the vent sites exhibits large sulfur isotope fractionation (>50‰), which indicates a close association between the vents and sulfate-reducing microbiota. In the subsurface, base metal sulfides precipitated from sulfide formed during the reduction of early diagenetic barite, also ultimately derived from seawater. This model suggests dynamic bottom-water redox conditions at the vent site driven by the interplay between sulfate-reducing organisms and metalliferous fluid effluence.

INTRODUCTION

Stratabound iron sulfides containing economically significant concentrations of base metals, commonly lead and zinc, constitute an important type of Mesoproterozoic metal deposit in sedimentary rocks. Models for their formation invoke metalliferous hydrothermal fluids venting into seawater or debouching into shallow sedimentary pore fluids and precipitating iron sulfides along stratiform horizons (Goodfellow et al., 1993; Large et al., 2005; Leach et al., 2010; Lydon, 1996; Russell et al., 1981). The preponderance of such deposits in Mesoproterozoic strata has been linked to increasing marine sulfate concentrations following the rise of atmospheric oxygen (Farquhar et al., 2010; Leach et al., 2010; Lydon, 1996; Lyons et al., 2006). Stratabound copper deposits are also tied to the Proterozoic oxygenation of Earth's surface (Hitzman et al., 2010). Curiously, despite their apparent synsedimentary or early diagenetic origins, many of these deposits lack obvious geological evidence for exhalative vents, such as a stockwork feeder zone or hydrothermal edifices (Large et al., 2005; Leach et al., 2005; Sangster, 2002), which could inform the chemistry of the hydrothermal fluids and seawater.

In this paper, we describe unusual structures composed of millimeter-scale tube-like features in the lower Mesoproterozoic Belt Supergroup at the site of the sediment-hosted Black Butte Copper Mine Project deposit, Helena Embayment, Montana (Fig. 1). Graham et al. (2012) first described the tube-shaped features, which they termed "net-textured pyrite," as decimeter-scale lenses and beds characterized by millimeter-scale ovoid pores bound by a network of fine-grained pyrite. These features represent three-dimensional connected networks, and here we refer to them as pyrite-walled tube structures. Amalgamations of the pyrite walls are overgrown by crystalline and euhedral pyrite and enclose tube-shaped spaces often filled by quartz, barite, or dolomite (Fig. 2).

Laminated pyrite around the Black Butte Copper Mine Project deposit is often crinkly and was therefore interpreted to represent mineralized microbial mats (Lyons et al., 2006; Schieber, 1989c, 1990). Pyrite interpreted to preserve microbial textures is also found associated with other sediment-hosted base metal deposits in Australia (Dunster, 1997; Ireland et al., 2004; McGoldrick, 1998, 1999; Oehler and Logan, 1977; Rohrlach et al., 1998). Tube structures at Black Butte are closely associated with crinkly pyrite and therefore might represent a

†ted@caltech.edu
§Present address: Department of Earth, Atmospheric and Planetary Sciences, Massachusetts Institute of Technology, 77 Massachusetts Avenue, Cambridge, Massachusetts 02139, USA.
#Present address: Department of Earth and Planetary Sciences, University of New Mexico, Albuquerque, New Mexico 87131, USA.
††Present address: Department of Earth and Planetary Science, University of California, Berkeley, 307 McCone Hall, Berkeley, California 94720, USA.
§§Present address: College of Earth, Ocean, and Atmospheric Sciences, Oregon State University, 104 CEOAS Administration Building, Corvallis, Oregon 97331, USA.

GSA Bulletin; March/April 2018; v. 130; no. 3/4; p. 598–616; https://doi.org/10.1130/B31504.1; 9 figures; 4 tables; Data Repository item 2017303; published online 12 September 2017.

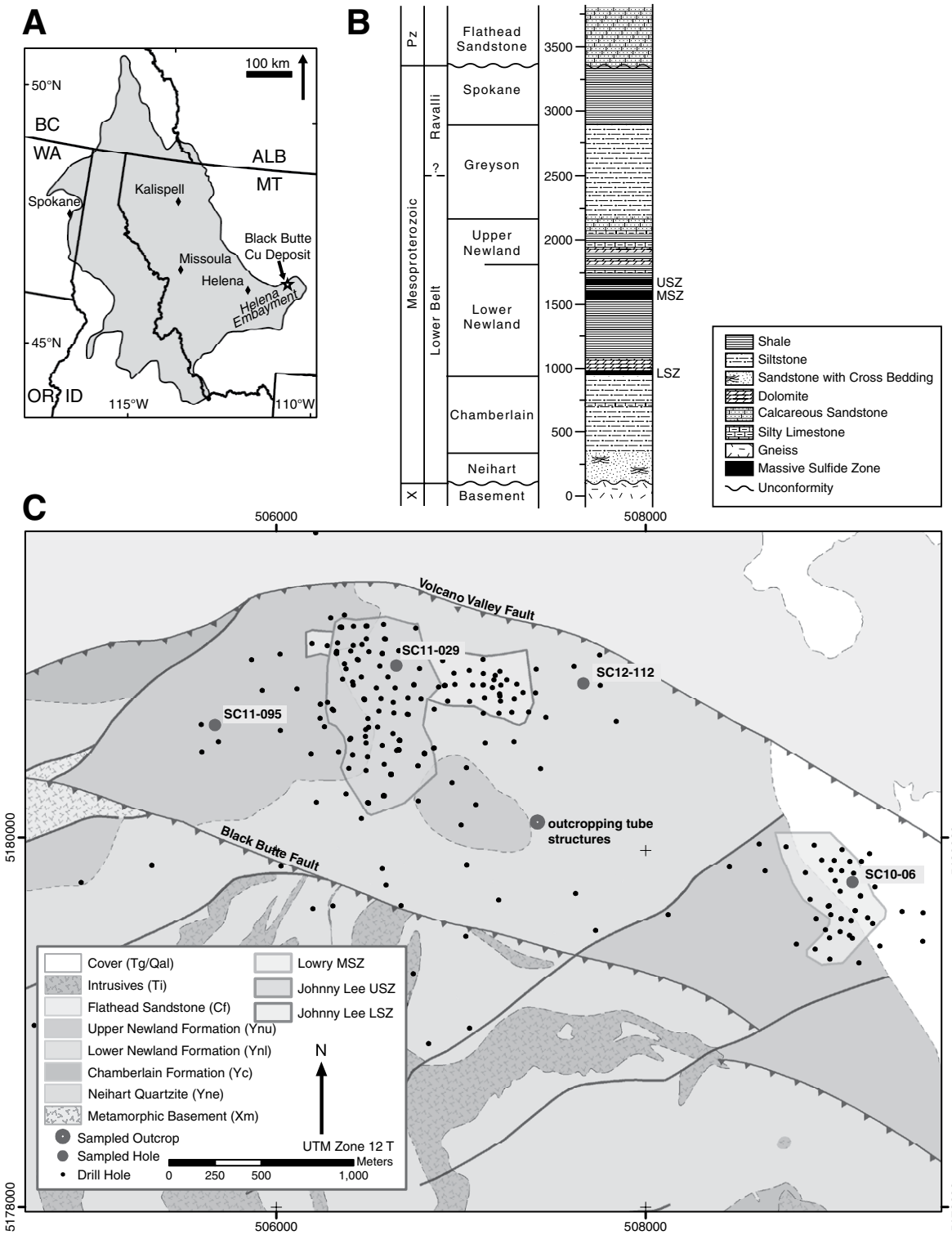

Figure 1. Geologic setting of the Black Butte Copper deposit, modified from Slotznick et al. (2015) with detailed map prepared by Tintina Resources, Inc. (A) Map of the Belt Supergroup outcrop limit. Star marks the location of the Black Butte Copper Mine Project (Cu) deposit within the Helena Embayment. BC—British Columbia; ALB—Alberta; WA—Washington; MT—Montana; OR—Oregon; ID—Idaho. (B) Lithostratigraphy of the Helena Embayment near Black Butte, with height in meters. USZ—upper sulfide zone, MSZ—middle sulfide zone, LSZ—lower sulfide zone, X—Paleoproterozoic Era, Pz—Paleozoic Era. (C) Geologic map of the Black Butte region (Universal Transverse Mercator [UTM] zone 12 T, World Geodetic Survey 1984 [WGS84] datum). Dots mark all locations drilled by Tintina Resources, Inc., or Cominco American, Inc. Drill cores and outcrops sampled for this study are labeled.

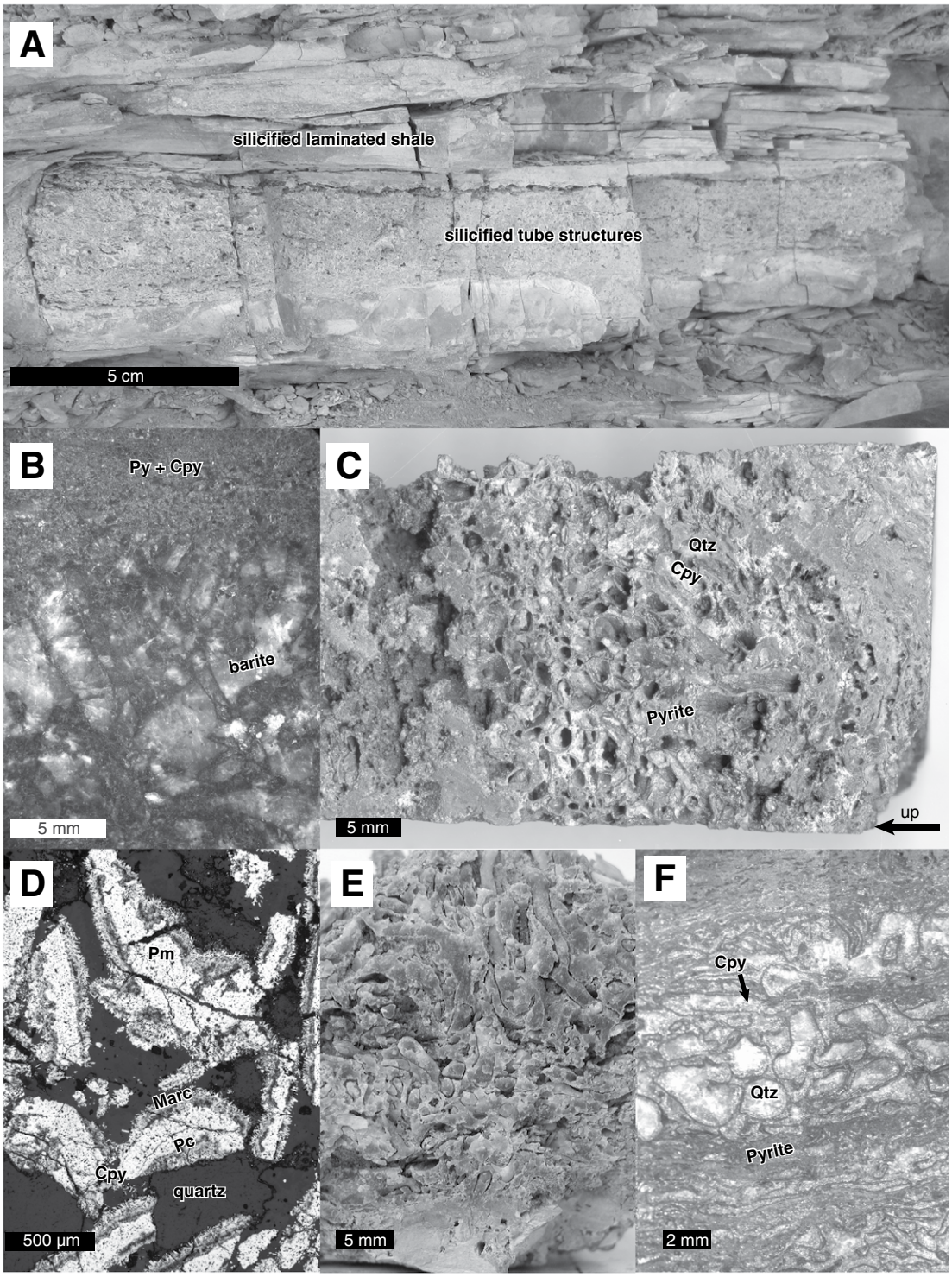

Figure 2. Pyrite-walled tube structures. (A) Outcrop photograph of decimeter-scale lens of tube structures in silicified gossan. (B) Core photo of subvertical pyrite-walled tube structures cemented by barite from drill core SC11-095-410.11–410.09 m. (C) Core photo of SC11-029-56.50–56.44 m (micro–computed tomography sample B1) with primary porosity partly occluded by chalcopyrite and euhedral quartz. (D) Fragments of tube structures with marcasite coating, SC11-029-76.35 m. (E) Tube structures that lack pyrite walls collected from the silicified gossan outcrop. (F) Photomosaic of tube structures showing spatial zonation of diameter, with the largest tubes clustered in the center of a region of narrower tubes. Tubes are filled with quartz that is rimmed by chalcopyrite. Py—pyrite, Cpy—chalcopyrite, Qtz—quartz, Pm—mottled pyrite, Marc—marcasite, Pc—Colloform pyrite.

novel morphology of a permineralized microbial community (McGoldrick and Zieg, 2004). However, close spatial association with microbial communities does not by itself provide evidence that the tube structures were built biologically (e.g., Grotzinger and Knoll, 1999).

While intermittently present near the Black Butte Copper Mine Project deposit, porous pyrite structures have, to the best of our knowledge, only rarely been described in other sediment-hosted deposits. The Paleoproterozoic Walford Creek deposit includes millimeter-scale "open-framework" pyrite interpreted as microbialites (Rohrlach et al., 1998); the Mesoproterozoic Gaobanhe deposit contains centimeter- to decimeter-scale pyrite chimneys (Li and Kusky, 2007); and the Carboniferous Ballynoe deposit contains millimeter-scale "curtains and sheaves" associated with hydrothermal vent chimneys (Boyce et al., 1983; Larter et al., 1981; Russell et al., 1989). More frequently, at least in Phanerozoic deposits, recognition of hydrothermal vent structures hinges on the occurrence of fossilized worm (animal) tubes (Banks, 1985; Boyce et al., 2003; Campbell et al., 2002; Moore et al., 1986), and these are often found in deposits hosted in volcanic rather than sedimentary rocks (Haymon et al., 1984; Little et al., 1997, 1998, 1999a, 1999b). However, if formed biologically, millimeter-scale structures in Mesoproterozoic rocks would necessarily indicate a novel mode of bioconstruction, and therefore assumptions about their genesis should be examined.

Based on physical, mineralogical, and isotopic analyses at the outcrop, drill core, and microscopic scale, we argue that the Black Butte tube structures represent local sites of hydrothermal fluid effluence to the seafloor in the Helena Embayment. This, in turn, suggests that the tube structures reflect syngenetic mineralization at the site of hydrothermal fluid venting and, thus, record paleoenvironmental information about the Belt Basin seawater and hydrothermal system. While isotopic data indicate that microbial sulfate reduction was an important source of sulfide for early pyrite deposition at Black Butte, this does not require that the tubes were accreted biologically; they could, as well, indicate abiotic precipitates colonized by bacterial communities.

GEOLOGIC SETTING

The Black Butte zinc-poor, copper-cobalt–rich sediment-hosted deposit occurs in the lower Newland Formation within the northern Helena Embayment, a syndepositional graben extending eastward from the center of the Mesoproterozoic lower Belt-Purcell Basin (Fig. 1A). The Newland Formation overlies the Neihart and Chamberlain Formations (Fig. 1B); the latter represent a fluvial/eolian sand blanket and supra-wave-base silty carbonaceous shale, respectively (Godlewski and Zieg, 1984; Schieber, 1989b; Winston and Link, 1993; Zieg, 1986; Zieg et al., 2013). The Neihart Formation is a coarse to very coarse, mature, hematitic quartz arenite with increasing very fine micaceous sand and silty shale as it grades into the overlying Chamberlain Formation (Schieber, 1989b). Correlation of the Newland Formation to the Prichard Formation to the northwest indicates a depositional age of ca. 1470 Ma (Aleinikoff et al., 2015; Graham et al., 2012; Sears et al., 1998). The lower Newland Formation marks rapid deepening associated with graben formation and consists of sub-wave-base laminated calcareous to dolomitic shale with intercalated conglomeratic debris flows and turbiditic sandstones. The upper Newland Formation and overlying lowermost Greyson Formation comprise two sub-wave-base carbonate-to-siliciclastic cycles. The Greyson Formation features relatively shallower, sub- and supra-storm-wave-base siltstones (Zieg, 1986).

In Late Cretaceous time, the south-dipping reverse Volcano Valley fault truncated pre–mid-Cambrian south-dipping (possibly Mesoproterozoic and/or synsedimentary) normal faults (Fig. 1C). Reverse faulting duplicated the lower Newland Formation in the Black Butte area and thrust lower Newland rocks over unconformably overlying mid-Cambrian rocks (Graham et al., 2012; Zieg et al., 2013). The Black Butte Copper deposit includes multiple stratabound sulfide zones in the Newland Formation, five of which are enriched in Cu, Co, and Ag. Three are economically important (Fig. 1C). Two, the upper sulfide zone and middle sulfide zone, occur in the hanging wall of the Volcano Valley fault. The third, the lower sulfide zone, is found in both the footwall and hanging wall of the Volcano Valley fault, is resource quality in the footwall, and is bounded on the north by one of the south-dipping normal faults, called the Buttress fault (Graham et al., 2012).

MATERIALS AND METHODS

Samples were collected from both outcrop and four subsurface cores previously drilled and stored in the Black Butte area by Tintina Resources, Inc., White Sulphur Springs, Montana (Fig. 1C). Mineralogical and textural characterization of pyrite-walled tube structures was accomplished by reflected light petrography of 15 thin sections, binocular microscopy of 27 drill-core segments, and centimeter-scale logging of a 6-m-long core segment. Qualitative elemental compositions and compositional contrasts were validated with electron dispersion spectroscopy and backscatter electron microscopy using a ZEISS 1550VP field emission scanning electron microscope (SEM) at the Caltech Geological and Planetary Sciences Division Analytical Facility, Pasadena, California, and with synchrotron-based X-ray fluorescence and absorption near-edge spectroscopy (Slotznick et al., 2015).

Three-dimensional morphology, porosity, density, and connectivity of the tube structures were determined using micro–computed tomography (micro-CT), a nondestructive, micron-scale, three-dimensional imaging method. Scanning was completed using an X-ray tube tomography system with a tungsten X-ray source (X-TEK HMX-ST 225, Nikon Metrology) at the Center for Nanoscale Systems at Harvard University, Cambridge, Massachusetts. The scans were completed at 115–190 kV source voltage, 42–135 μA source current, 0.1–2.0 mm copper filter, and 1–2 s integration time, with ~2100–3200 frames acquired over 360°, and ~2 h scan time per sample. Three-dimensional reconstructions were generated using CTPro (Metris) and VGStudio Max 2.0 (Volume Graphics). We identified internal volumes (hypothesized pores) from the reconstructions by using density differences with the surrounding material (Supplemental Fig. DR1[1]). We used an edge-preserving, curvature-driven algorithm in Avizo Fire 8.1 (FEI) to filter potential pore networks, an interactive thresholding process that characterized potential pores' sizes and orientations; pores were separated and given unique labels. Length, width, aspect ratio, volume, and orientation data were then extracted for all pores using Avizo Fire. Pore orientation data were analyzed with the RFOC Spherical Statistics and R Stats packages (Lees, 2014; R Core Team, 2015).

Two Black Butte samples were scanned: (1) sample B1, an upper sulfide zone sample with pyrite walls and open pores from drill-core SC11-029-56.5 m (Fig. 2C); and (2) sample B3, a silica-replaced outcrop sample from 46°46.368′N, 110°52.843′W above upper sulfide zone gossan (Fig. 2A).

In addition, three samples from potential modern analogs were analyzed: (1) sample M1, an anhydrite-walled chimney from a 300–311 °C vent called "Hot Harold" in the Mothra vent field on the Juan de Fuca Ridge (collected during HOV *Alvin* cruise AT-15–23 on 9 September 2007 at 47°55.42566′N, 129°6.49176′W, 2278 m depth); (2) sample

[1]GSA Data Repository item 2017303, Appendix 1, Supplementary Figures DR1–DR4, and Movie Files B1, B2, M1, LCL, and LCM, is available at http://www.geosociety.org/datarepository/2017 or by request to editing@geosociety.org.

LCL, an inactive carbonate-walled chimney (sample 3871-1442 collected during HOV *Alvin* cruise AT-7-41 [Sample LCL was collected at 30°07.380′N, 42°07.060′W on 6 May 2003]) in the Lost City Hydrothermal Field; and (3) sample LCM, a carbonate-walled flange called "IMAX" on a 53–60 °C vent on the Poseidon structure in the Lost City Hydrothermal Field (sample 3869-1404 collected at Marker 2 during HOV *Alvin* cruise AT-7-41 [Sample LCM was collected at 30°07.423′N, 42°07.200′W on 4 May 2003]; Bradley, 2008; Bradley et al., 2009; Kelley et al., 2005). The Mothra vent field is a high-temperature hydrothermal complex of steep-spired pyrite and sulfate chimneys in the axial trench of the Juan de Fuca Ridge, and the Hot Harold sample (M1) comes from an active, fault-controlled vent that is younger than the last eruptive basaltic dike emplacement on the ridge (10^2–10^3 yr; Glickson et al., 2007; Kelley et al., 2001a; Lin et al., 2016). The Lost City Hydrothermal Field (samples LCL and LCM) is a long-lived (10^5 yr), lower-temperature hydrothermal system driven by exothermic serpentinization reactions of peridotite exposed by detachment faulting in the Atlantis Fracture Zone, off-axis of the slow-spreading Mid-Atlantic Ridge (Früh-Green et al., 2003; Kelley et al., 2001b, 2005; Ludwig et al., 2006).

Sulfide-sulfur isotopic compositions of pyrite and chalcopyrite were determined on two thin sections (SC11-029-56.42 m and SC11-095-389.22 m) by secondary ion mass spectrometry (SIMS) on a Cameca 7f-Geo at the Caltech Microanalysis Center. One inch (2.5 cm) round polished thin sections (25 µm thick) were prepared from sections of drill core (Supplemental Fig. DR2 [see footnote 1]) and examined with a polarizing reflected light microscope, backscatter electron microscopy, and energy dispersive electron spectroscopy to understand the microtexture of the pyrite-walled tube structures and to select analysis sites for in situ sulfide-sulfur isotope measurements. The sections were then coated with 30 nm of gold using a Cressington sputter coater. A 19 kV $^{133}Cs^+$ primary beam was used to presputter an ~100 µm^2 surface with an ~3 nA current. The same primary beam with a 1–3 nA current was used to acquire 10 cycles of ^{32}S for 0.96 s and ^{34}S for 2 s on an ~25 µm^2 spot; typical count rates were ~10^9 counts per second (cps) for ^{32}S and ~10^8 cps for ^{34}S. Mass resolution was between 3000 and 4500 to ensure measured ^{34}S intensities were at least 10^5 times the intensity of the ^{33}SH isobaric interference. For each analysis, two standard deviation (s.d.) outliers were culled from the 10 cycles. Measured ratios were converted to the Vienna-Canyon Diablo Troilite (V-CDT) isotopic reference scale by bracketing blocks of ~16 analyses with sets of 4 analyses of an in-house pyrite standard mounted and polished in the thick section (Fischer et al., 2014; Johnson et al., 2013). Ablation pits in pyrite and chalcopyrite were accurately determined relative to the pyrite standard. Reproducibility of $^{34}S/^{32}S$ of the in-house pyrite standard was typically 0.3‰–0.7‰ (2σ standard error [s.e.]) for each block. Galena was analyzed precisely, but we did not embed an in-house galena standard in the thin sections, so the accuracy of the measurements was subject to matrix effect biases (Kozdon et al., 2010).

Texture-specific sulfate-sulfur isotopic compositions of barite and carbonate-associated sulfate (CAS; e.g., Burdett et al., 1989) in dolomite were determined on microdrilled powders from polished drill-core slabs from all three sulfide zones. Ten milligrams of silty dolomite or 50–300 µg of barite were precleaned by sonicating for 4 h in a 10% (w/w) NaCl solution and then rinsing three times in Milli-Q water (Millipore), centrifuging, and removing the supernatant between each step (Present et al., 2015). Carbonates were dissolved in 0.5 *N* trace-metal pure HCl (Seastar Baseline), and barites were dissolved by exchange with a concentrated $NaCO_3$ solution (Breit et al., 1985). Sulfate was purified from other ions with a Biorad AG-1-X8 anionic exchange resin before analysis in duplicate as aqueous sulfate by multicollector–inductively coupled plasma–mass spectrometry (MC-ICP-MS) on a Thermo Finnegan Neptune Plus at Caltech (Paris et al., 2013, 2014). Analysis by this method requires matrix-matching samples to an in-house Na_2SO_4 bracketing standard. To do this, an appropriate amount of NaOH solution was added to samples; their sizes were determined to be 5–300 nmol of sulfate by ion chromatography with a Dionex ICS-2000 on an AS-19 column using 20 m*M* KOH eluent at the Caltech Environmental Analysis Center. Due to instrument instability when these analyses were performed, precision of $\delta^{34}S$ measurements of sulfate was generally between 0.2‰ and 1.4‰ (1σ s.e.). Analytical procedural blanks were 0.4 ± 0.28 nmol S (1σ standard deviation [s.d.]).

TUBE LITHOLOGY, MORPHOLOGY, AND TEXTURE

Lithofacies

Pyrite-walled tube structures and associated sediments in the upper sulfide zone were logged at centimeter scale in core SC11-095 between 412.07 m and 406.07 m, where tube structures are abundant (Fig. 3). Tube structures occur within the pyrite lithofacies, which are closely associated with laminated striped shale and breccia lithofacies (Graham et al., 2012).

Pyrite Lithofacies

Tube structures occur within decimeter-thick intervals of mottled and porous fine-grained pyrite (Figs. 4A, 4B, and 4C). The fine-grained pyrite occurs as polyframboid aggregates (cf. Love, 1971), or as clotted pyrite in a barite or silt matrix. Aggregates consist of sub-millimeter spheroidal clusters of coalesced 5–25 µm pyrite grains (cf. type PD; Himes and Peterson, 1990). Clots are larger clusters of pyrite aggregates, up to 1 mm in size, with irregular spheroidal or ovoid form, and dark color. These textures are often mingled with small irregular incipient tubes that grade up into well-developed tube structures (arrow in Fig. 4A). In some cases, layers of fine-grained, crinkly laminated sulfide minerals enclose or are interbedded with tube-bearing buildups (Figs. 4A and 4C). The crinkly laminated fabric is defined by: pyrite/chalcopyrite aggregates and clots; barite-filled irregular voids; and rare, millimeter-sized incipient tubes.

The best-expressed tube structures are up to 3 mm in diameter with irregular shape and finely crystalline sulfide walls ~100 µm thick (Fig. 2). Sulfide walls often are discontinuous and have a preferential subvertical orientation (Figs. 2B, 2C, and 2E). The largest tubes cluster to form concentrations normal to bedding (Fig. 2F). Coarser sulfides overgrow the walls. Chalcopyrite, dolomite, barite, and/or quartz often fill the tube structures and polygonal spaces between them; uncommonly residual porosity is preserved (Figs. 2C and 4C). In outcrop, silica completely fills the tubes, and pyrite is no longer present (sample B3 and Figs. 2A and 2E).

Centimeter-sized laths and veins of a late-stage barite may pervasively overgrow pyrite lithofacies, especially where early diagenetic barite laths dominate interstratified shales (Graham et al., 2012).

Laminated Striped Shale Lithofacies

Carbonaceous, thinly laminated quartz/dolomite siltstone and very thinly bedded quartz silt to dolomite mud graded couplets (Fig. 4D) characterize this facies (Graham et al., 2012; Schieber, 1989a; Zieg, 1986). Disseminated pyrite—including nodules similar to the clots and aggregates in the crinkly laminated pyrite—and irregular-shaped lenses of fine-grained pyrite are ubiquitous. Light-gray silty intervals containing 1–2 mm black mud chips form wavy beds up to 3 cm thick. Dolomite is finely crystalline, and some beds show recrystallization into nodules associated with minor fractures that are filled with siliciclastic mud. Laminae are planar to slightly wavy where compacted around nodules (Fig. 4D); their bases are either sharp or scoured. Wavy-bedded mudstone forms partings up to 3 cm thick.

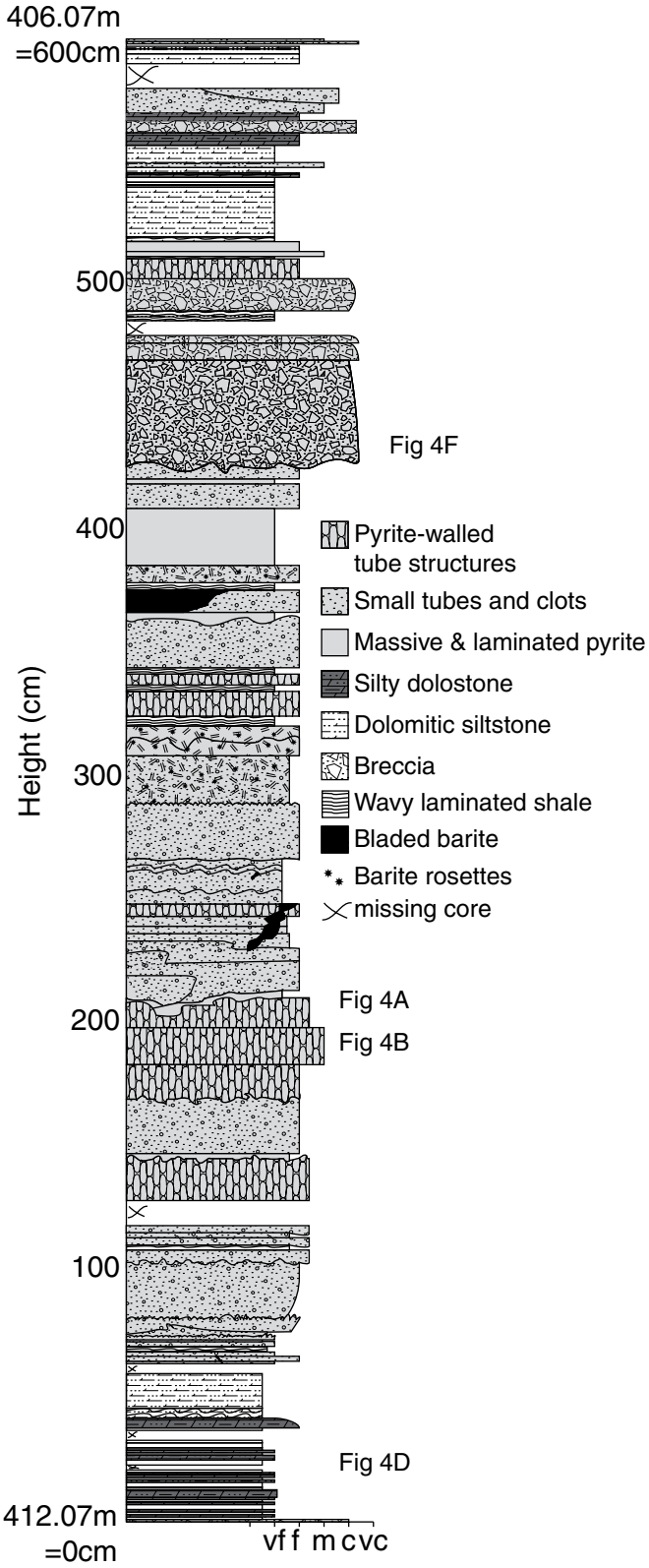

Figure 3. Lithostratigraphic log of core SC11-095 between 412.07 m (base of section) and 406.07 m (top of section, at 600 cm); grain size: vf—very fine; f—fine; m—medium; c—coarse; vc—very coarse. Where indicated, photographs of the core are shown in Figure 4.

Early diagenetic barite laths up to 1 cm long displace the laminated striped shale facies and tend to be concentrated within particular intervals. Compaction around laths and pyrite nodules deformed silt beds and disrupted fine-grained pyrite lenses (Fig. 4E).

Breccia Lithofacies

Both matrix- and clast-supported sedimentary breccias contain poorly sorted, angular granule- to cobble-sized clasts of the laminated striped shale and pyrite lithofacies (Fig. 4F; Supplemental Figs. DR4B, DR4D, and DR4F [see footnote 1]). The latter include pyrite-walled tube structures, indicating that they formed prior to resedimentation. The matrix is variably composed of dolomite, silty shale, and fine-grained pyrite. The breccia lithofacies is often overlain by pyrite-walled tube structures (arrow in Fig. 4F) in the pyrite lithofacies.

Three-Dimensional Morphology

The two Black Butte micro-CT reconstructions show broadly similar three-dimensional tube morphology featuring arcuate pores with rounded ends and a tendency to form centimeter-scale clusters. This is best illustrated by the subsurface sample that has minimal occlusion of tube porosity (sample B1; Figs. 2C, 5A, 5D, and 5G; Supplemental Movie B1 [see footnote 1]) due to the strong density contrast between open pores and the pyrite walls. Tubes sampled from the gossan outcrop (sample B3; Supplemental Movie B3 [see footnote 1]) are completely silicified, and original wall material—presumably pyrite—is absent (Figs. 2A and 2E).

The Lost City samples (LCL and LCM) show very similar three-dimensional anastomosing pore morphologies, including smooth-walled, arcuate pores with rounded terminations (Figs. 5B, 5E, and 5H; Supplemental Movies LCL and LCM [see footnote 1]). The Juan de Fuca sample (M1), featuring tubes formed by anhydrite walls, shows numerous laterally linked small pores that produce an overall porous texture, and fewer larger fluid-flow paths (Figs. 5C, 5F, and 5I; Supplemental Movie M1 [see footnote 1]). Reconstructions were challenging because the small pores are difficult to resolve individually, while larger fluid-flow paths are generally not fully enclosed within the sample. Although they are not well suited for the micro-CT porosity reconstruction method used here, we included these data.

Quantifiable characteristics of porosity include the length, width, aspect ratio, and orientation of individual pore spaces. We measured these characteristics for hundreds of pores in each sample, and the mean and standard

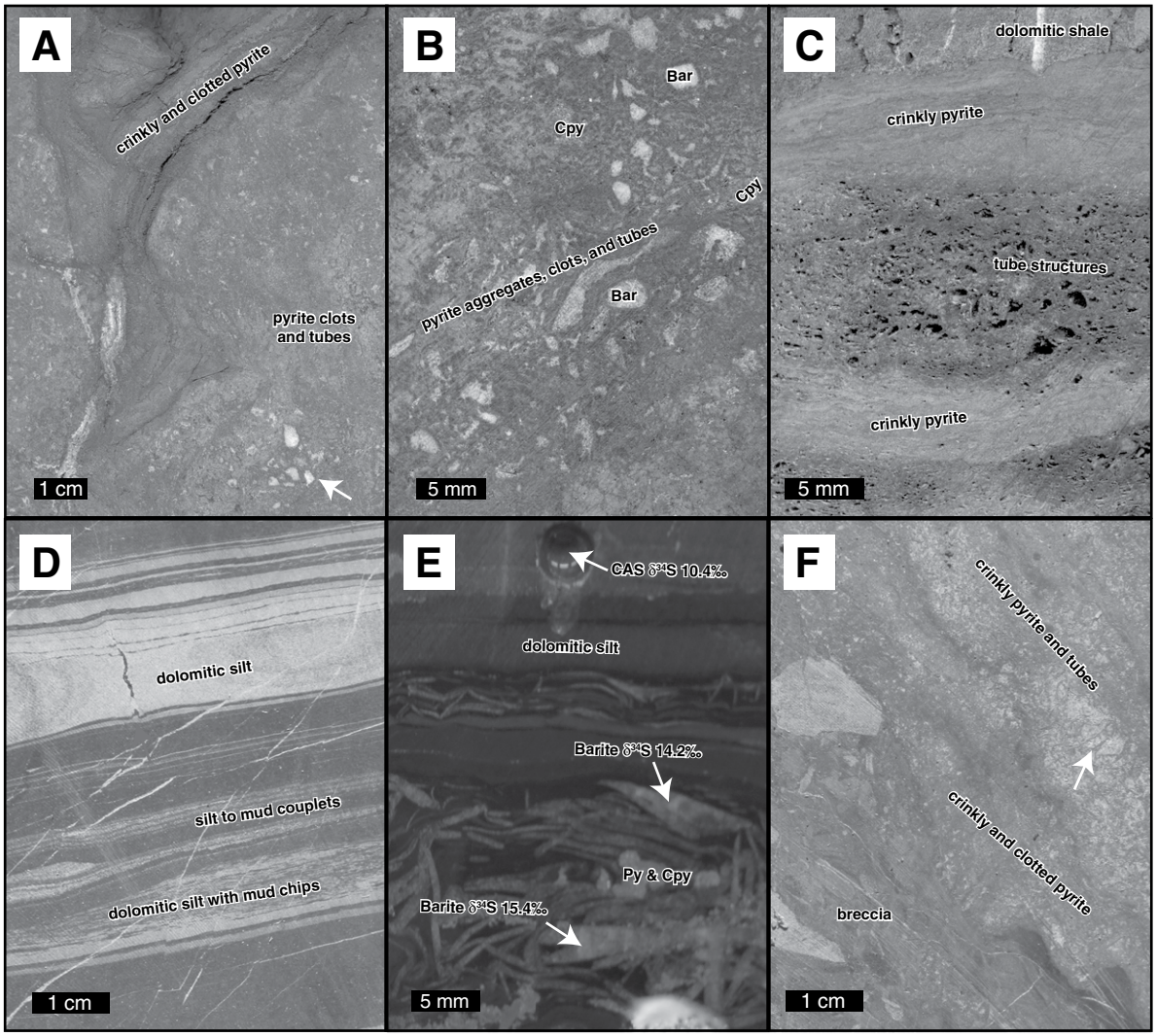

Figure 4. Representative examples of the lithofacies associated with pyrite-walled tube structures from vertical cuts through drill core. (A) SC11-095 drill-core intercept of the upper sulfide zone at 410.02 m, showing the pyrite lithofacies with barite-filled irregular pyrite-walled tube structures that are overgrown by coarse pyrite. Note the three-dimensional structure defined by crinkly pyrite with larger pyrite-walled tube structures near its core (arrow) and finer poorly laminated pyrite along its edges. (B) SC11-095 drill core at 410.17 m, showing clotted and porous pyrite lithofacies with barite-filled pores and tube structures, and some replacement by chalcopyrite. (C) SC11-029 drill core at 76.20 m, showing tube structures intercalated with crinkly laminated pyrite in the pyrite lithofacies. (D) SC11-095 drill core at 411.97 m, showing laminated striped shale lithofacies, with graded lamina, recrystallization of dolomite into protonodules with fracture prior to compaction, dolomitic siltstone with small mud chips, and barite-filled high-angle fractures with reverse offset. (E) Dolomitic cap of graded laminations and synsedimentary barite rosettes being replaced by pyrite in the upper sulfide zone from core SC11-029, 61.185 m. The sulfur isotopic composition of silty dolomite carbonate-associated sulfate (CAS) samples is lighter than that of barite samples. (F) SC11-095 drill core at 407.77 m showing pyrite-walled tube structures (arrow) and barite laths underlain by clast-supported breccia lithofacies with a pyrite-rich matrix. Py—pyrite; Bar—barite; Cpy—chalcopyrite.

deviation of quantifiable characteristics are reported in Table 1. Visual analysis of reconstructed pore networks showed that tube structures have pore volumes equal to or greater than 0.05 mm^3 (e.g., Figs. 5G–5I). A comparison of pore characteristics indicated a similar range of pore sizes between the Black Butte structures and the modern chimney fluid-flow structures (Table 1). All had similar lengths (~2–3 mm) and widths (~1 mm), with mean dimensions indistinguishable within one standard deviation. The orientation of the pores was calculated by measuring the trend (Θ) and plunge (Φ) of the long axes relative to arbitrary horizontal axes and a vertical axis. The samples that we analyzed exhibited predominantly subvertical pores that plunged steeply with respect to bedding. However, some pyrite-walled tube structures from other Black Butte samples appeared to be oriented more horizontally and may have been crushed or flattened (Graham et al., 2012).

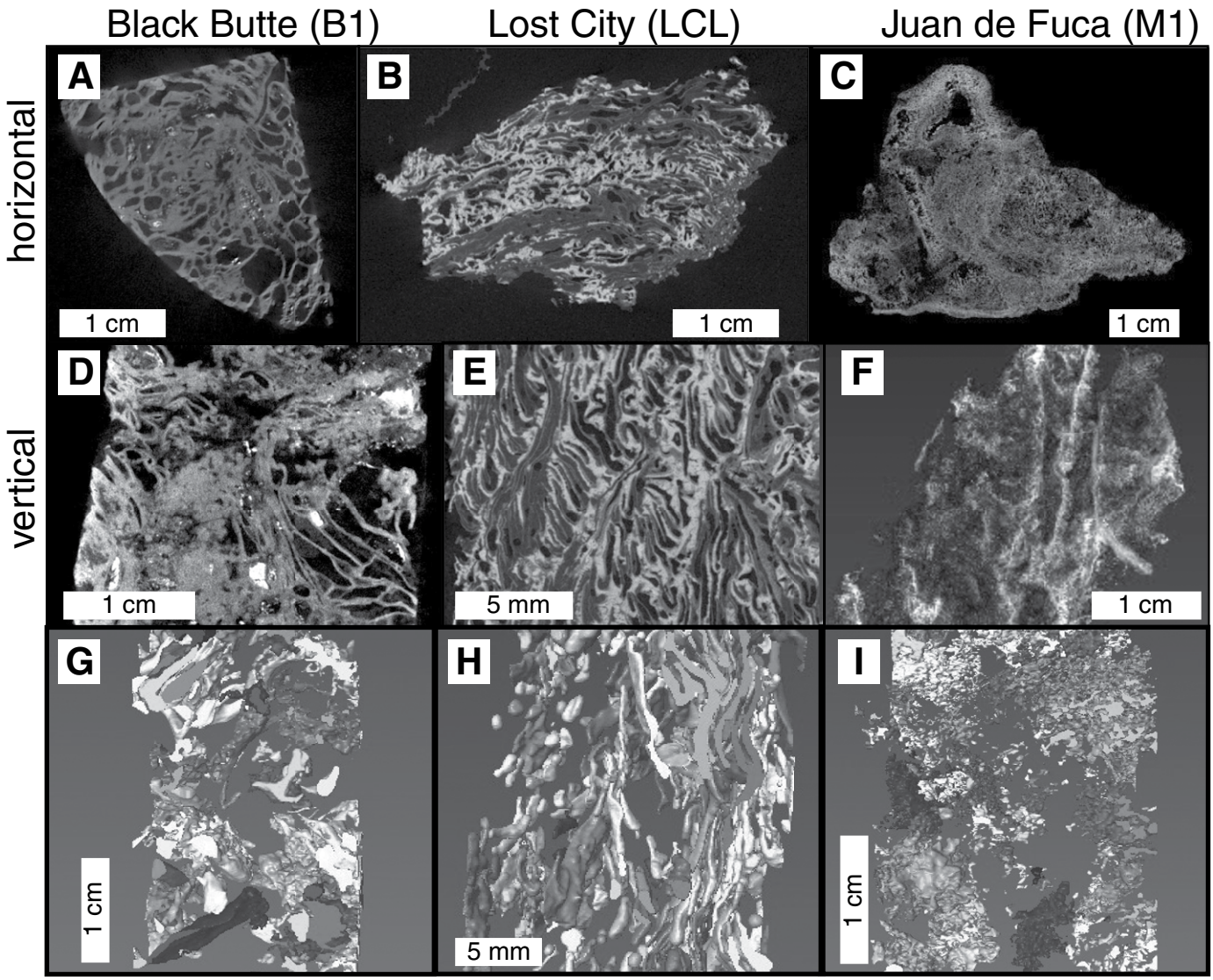

Figure 5. Micro–computed tomography reconstructions of the three-dimensional porosity structure. (A) Grayscale density image of the Mesoproterozoic Black Butte subsurface sample B1 in the horizontal plane, with the brightest white indicating the densest sulfide phases. (B) Grayscale density image of the modern carbonate-brucite–walled sample LCL from Lost City in the horizontal plane, with the brightest white indicating the densest carbonate. (C) Grayscale density image of the modern anhydrite-walled structure M1 from the Juan de Fuca Ridge in the horizontal plane, with the brightest white indicating the densest anhydrite. (D–F) Vertical cross sections of the three samples described above. (G–I) Subset of pores reconstructed from each of the above samples by hiding material denser than a threshold, with volume ≥0.05 mm^3; each highlights characteristic features of the sample. Grayscale differentiates nearby pores and does not indicate connectivity between pores of the same tone. (G) Subset of reconstructed pores from Black Butte sample B1 that have any trend, and a long-axis plunge of 45°–65°. Bedding in this section of drill core dips 55° relative to the core axis that defines the vertical axis of reconstruction, so these pores had a subvertical paleo-orientation. (H) Subset of reconstructed pores from Lost City sample LCL that have any plunge and a long-axis trend in the same 100°-wide arc. (I) Subset of reconstructed pores from Juan de Fuca Ridge sample M1 that have any trend and a long-axis plunge of 34°–75°. The largest subvertical fluid conduits are not enclosed by the sample.

Paragenesis

Paragenesis of pyrite-walled tube structures in the upper sulfide zone occurred in three main stages (Fig. 6A). In the first stage, abundant disseminated fine-grained pyrite and pyrite nodules formed within surface sediments, and early diagenetic barite laths precipitated. Second, tube walls precipitated as constructional edifices at the sediment-water interface, possibly as a metastable sulfide, hydroxide, carbonate, or sulfate. Mottled pyrite and colloform pyrite soon replaced the original mineralogy of the tube structures. In some cases, euhedral marcasite overgrew the tube structures (Fig. 2D). Third, these textures were infilled by massive barite. Dolomite and quartz occluded most remaining porosity and replaced the massive barite (Graham et al., 2012). Barite, dolomite, quartz, and the earlier pyrite textures associated with tube structures were in turn overgrown or replaced

TABLE 1. MICRO–COMPUTED TOMOGRAPHY QUANTIFICATION RESULTS

Sample	*n**	Length (mm)	Width (mm)	Aspect ratio	Volume (mm^3)	Length Φ† (°)	Length Θ§ (°)	Width Φ (°)	Width Θ (°)
B1 (Black Butte core)	470	3.49 ± 2.00#	1.53 ± 0.99	2.46 ± 0.85	2.84 ± 4.78	55 ± 21	182 ± 94	60 ± 22	174 ± 106
B3 (Black Butte outcrop)	308	3.26 ± 2.66	1.57 ± 1.40	2.29 ± 0.62	2.13 ± 4.41	54 ± 22	268 ± 176	64 ± 20	159 ± 102
M1 (Juan de Fuca Ridge)	740	2.18 ± 1.68	1.02 ± 0.88	2.25 ± 0.57	1.38 ± 5.35	55 ± 21	182 ± 102	59 ± 22	174 ± 98
LCL (Lost City, inactive)	904	1.92 ± 1.41	0.68 ± 0.35	2.74 ± 1.04	0.36 ± 0.53	47 ± 22	170 ± 95	66 ± 17	185 ± 99
LCM (Lost City, active)	371	2.46 ± 1.45	0.90 ± 0.53	2.88 ± 1.00	0.53 ± 0.94	49 ± 23	158 ± 85	59 ± 23	206 ± 104

*Number of pores with reconstructed volume greater than 0.05 mm^3.
†Angle between the pore's axis and the z axis (i.e., plunge), between 0° and 90°.
§Angle between the pore's axis and the x axis (i.e., azimuth), between 0° to 360°.
#Uncertainties tabulated as one standard deviation.

by coarse pyrite and base metal minerals (Graham et al., 2012). These textures are described in Table 2 and illustrated in Figure 7.

Gangue mineralogy differs significantly among sulfide zones (Graham et al., 2012; Zieg et al., 2013). In the upper sulfide zone, carbonate occurs as fine sediment in the laminated striped shale lithofacies (Fig. 4D; Supplemental Figs. DR3A and DR3E [see footnote 1]), as dolostone clasts in the breccia lithofacies (Fig. 4F; Supplemental Figs. DR3B, DR3D, DR3F, and DR3G [see footnote 1]), as dolomite rims and overgrowths on quartz, and as coarse dolomite cement filling porosity (Fig. 8A). Barite forms early diagenetic laths that precipitated in the laminated striped shale lithofacies prior to sediment compaction (Fig. 4E; Supplemental Figs. DR3C and DR3D [see footnote 1]), and as later veins and laths that occlude porosity (Supplemental Figs. DR3F and DR3G [see footnote 1]). Quartz occurs as veins crosscutting all of the pyrite generations (Fig. 7G), and as porosity-occluding subhedral crystals that fill the pyrite-walled tube structures (Figs. 2B, 2C, 2F, 8B, and 8C); it is often rimmed by coarse irregular pyrite (Fig. 8B). Quartz is also closely intergrown with the colloform pyrite (Figs. 8B and 8D).

Sulfur Isotope Results

The sulfur isotopic composition of CAS and early diagenetic barite laths was determined in samples microdrilled from eight polished slabs

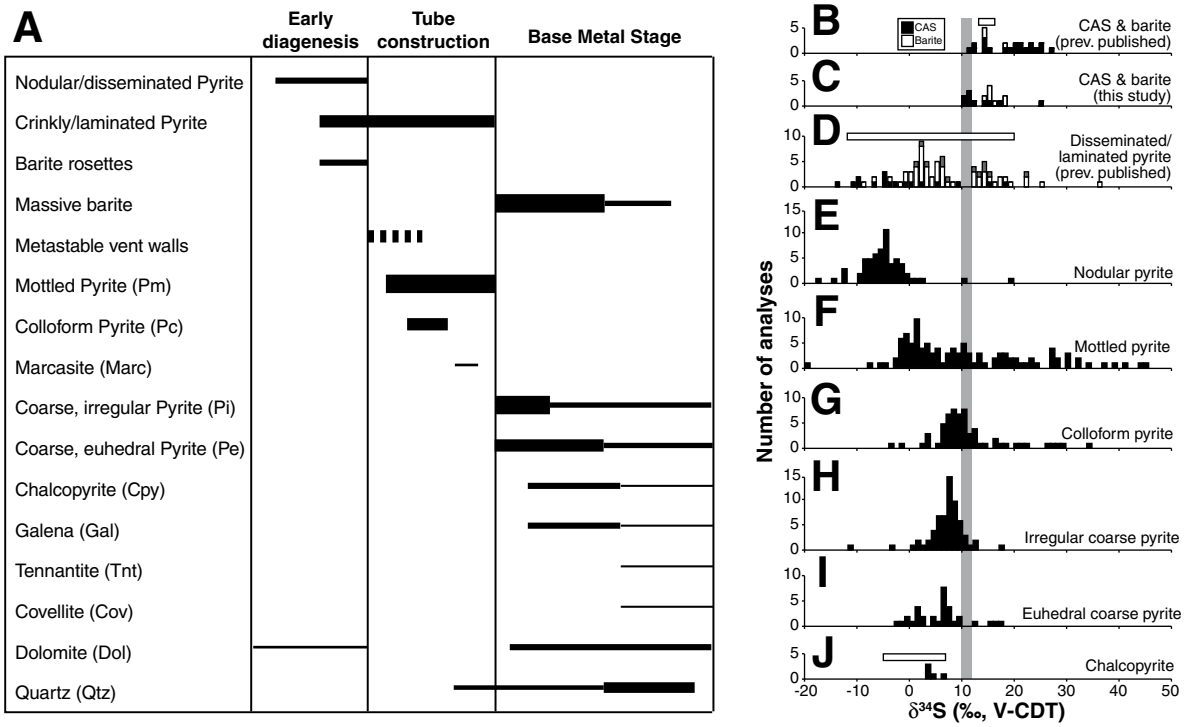

Figure 6. (A) Paragenesis of tube structures and associated rocks from the upper sulfide zone. Phases with thicker bars are qualitatively more abundant. Dashed bar for metastable vent walls indicates that the phase is inferred but no longer present (see text for details). (B–J) Histograms of sulfur isotope data from the literature and this study. White horizontal bars are data ranges reported by Zieg and Leitch (1998) for barite, laminated pyrite, and chalcopyrite. Data in B were compiled from Gellatly and Lyons (2005), Strauss (1993), and Strauss and Schieber (1990). Data in D were compiled from Strauss and Schieber (1990, black), Lyons et al. (1993, gray), and Lyons et al. (2000, white). Gray shaded region highlights the interpreted sulfur isotopic composition of seawater sulfate in the Helena Embayment during deposition of the Newland Formation (see text for details). CAS—carbonate-associated sulfate; V-CDT—Vienna-Canyon Diablo Troilite.

TABLE 2. SULFIDE TEXTURES IN PYRITE-WALLED TUBE STRUCTURES AND RELATED LITHOFACIES

Sulfide texture	Description
Disseminated pyrite	Anhedral (occasionally framboidal) pyrite crystallites less than 5 µm wide, often with euhedral overgrowths (Graham et al., 2012; Himes and Peterson, 1990; Schieber, 1989c; Strauss and Schieber, 1990; White et al., 2013).
Nodular pyrite (Pn)	Ovoid porous masses, up to 1 mm in diameter, of disseminated pyrite crystallites coalesced and/or encrusted by later euhedral pyrite (Graham et al., 2012; Himes and Peterson, 1990; Strauss and Schieber, 1990).
Colloform pyrite (Pc)	Botryoidal and isopachous fine-grained pyrite layers up to 5 µm thick; accreted both towards the interior of tube structures and away from the exterior tube wall surfaces into polygonal void spaces; often intergrown with quartz.
Mottled pyrite (Pm)	Clusters of anhedral to euhedral pyrite grains up to 25 µm in diameter (cf. type PB of Himes and Peterson, 1990) that are overgrown by brighter coarsely crystalline pyrite; abundant small (<2 µm) pores and inclusions of other sulfide minerals; intergrown with colloform pyrite; referred to as "spongy pyrite" by Graham et al. (2012).
Marcasite (Marc)	Coarse euhedral grains, often bladed, up to 40 µm long.
Coarse, irregular pyrite (Pi)	Bright, uniform, anhedral pyrite with embayed margins and numerous small (<2 µm) inclusions of galena, chalcopyrite, and tennantite; overgrows earlier pyrite stages by following colloform topography, fills crosscutting veins up to 10 µm wide, and rims quartz filling tube structures.
Coarse, euhedral pyrite (Pe)	Bright, uniform, subhedral to euhedral continuous overgrowth on coarse irregular pyrite; dominant sulfide occluding tube structure porosity; commonly contains exsolved anhedral blebs of chalcopyrite and galena.
Chalcopyrite (Cpy) and galena (Gal)	Porosity-occluding anhedral crystals; blebs up to 20 µm in diameter exsolved from coarse euhedral pyrite; smaller (<10 µm) anhedral grains replacing mottled and colloform pyrite.
Covellite (Cov)	Porosity-occluding anhedral crystals; chains of anhedral grains replacing chalcopyrite associated with colloform pyrite.
Tennantite (Tnt)	Porosity-occluding anhedral crystals.

from all three sulfide zones (Fig. 4E; Supplemental Fig. DR3 [see footnote 1]). Silty dolomite dissolved for CAS sulfur isotopic analyses was collected from the tops of graded silt-to-carbonate couplets from the laminated striped shale facies, and from silty dolomite clasts in the breccia facies. Barite and CAS sulfate isotopic compositions and concentrations (for CAS) are reported in Table 3.

Barite samples have a $\delta^{34}S$ composition of 14‰–18‰ V-CDT (open boxes in Fig. 6C). CAS samples have a composition of 10‰–25‰ V-CDT, but most samples are generally ^{34}S-depleted relative to the barite samples and have an isotopic composition of less than 13‰ V-CDT (solid boxes in Fig. 6C). A range of CAS $\delta^{34}S$ compositions of up to 4‰ was observed across short stratigraphic thicknesses in the laminated striped shale facies (Supplemental Fig. DR3A [see footnote 1]), and amongst co-occurring silty dolomite clasts in the breccia facies (Supplemental Fig. DR3B [see footnote 1]).

Sulfur isotopic measurements of the 10-µm-wide ablation pits in sulfide minerals are illustrated in Figure 8 and Supplemental Figure DR4 (see footnote 1). All data are tabulated in Appendix 1 (see footnote 1) and summarized in Table 4.

In situ sulfur isotope data from the tube structures and diagenetic pyrite nodules generally coincide with Newland Formation pyrite data reported previously (Fig. 6D; Lyons et al., 1993, 2000; Strauss and Schieber, 1990; Zieg and Leitch, 1998). Pyrite nodules have a mode of ~–5‰ V-CDT, with data right-skewed to values as high as 19‰ V-CDT (Fig. 6E). Mottled pyrite has a $\delta^{34}S$ mode of ~1‰ V-CDT, and the data are right-skewed to values as high as 45‰ V-CDT (Fig. 6F). Colloform pyrite has a mode of ~10‰ and is right-skewed to a value of 34‰ V-CDT (Fig. 6G). Coarse irregular pyrite and coarse euhedral pyrite each have a mode of ~6‰ V-CDT and symmetrically distributed values (Figs. 6H and 6I). Chalcopyrite grains were only large enough to measure in five locations, but they have a mean composition of 3.9‰ V-CDT (Fig. 6J).

DISCUSSION

Sulfur Biogeochemistry During Deposition of the Newland Formation

The presence of broken pyrite-walled tube structures as intraclasts in the breccia facies indicates that they formed in shallow sediments or above the sediment-water interface (Figs. 2D and 8A). They are also closely associated with crinkly laminated pyrite (Figs. 4A and 4C), which has been previously interpreted as a preserved microbial mat texture at Black Butte (Lyons et al., 2006; Schieber, 1989c, 1990). During deposition of the Newland Formation, deep water in the Black Butte area of the Helena Embayment was anoxic but contained sulfate (Planavsky et al., 2011; Slotznick et al., 2015). Sulfur isotope studies of disseminated and framboidal sedimentary sulfides (Figs. 6D and 6E) suggest that sulfate from the ocean fed microbial sulfate-reducing communities in shallow sediments (Lyons et al., 1993, 2000; Strauss and Schieber, 1990).

The isotopic composition of CAS and early diagenetic barite constrains the isotopic composition of seawater sulfate. In modern carbonates, CAS provides an accurate proxy for the isotopic composition of contemporaneous seawater sulfate (Burdett et al., 1989; Kampschulte et al., 2001; Lyons et al., 2004); however, for older strata, the fidelity of this archive is less certain (Present et al., 2015). Our data generally overlap with a compilation of previously published barite and CAS data for the Helena Embayment rocks (Figs. 6B and 6C; Gellatly and Lyons, 2005; Strauss, 1993; Strauss and Schieber, 1990; Zieg and Leitch, 1998). It is common in organic-rich marine sediments for sulfate reduction in sediment pore fluids to exceed the rate that sulfate can diffuse from seawater into the sediments; this leads to closed-system behavior during the kinetic fractionation of sulfate, and it enriches the residual pore-fluid sulfate in ^{34}S (Jørgensen, 1979). This behavior appears to be present in our sulfate $\delta^{34}S$ data. This interpretation is reinforced by the observation that the barite is generally higher in $\delta^{34}S$ relative to CAS by ~4‰ in samples where both barite and CAS were measured (Fig. 4E; Supplemental Fig. DR3 [see footnote 1]). Based on petrographic textures (Fig. 4E), diagenetic barite precipitated below the sediment-water interface from sulfate more likely to be diagenetically ^{34}S-enriched, while synsedimentary dolomite was more likely to preserve CAS values recording the original composition of seawater. Some CAS measurements are much heavier in $\delta^{34}S$ (up to 25‰ V-CDT; Supplemental Fig. DR3E [see footnote 1]), so it is possible that significant amounts of diagenetically high $\delta^{34}S$ sulfate may have been incorporated into the dolomite during recrystallization of a primary carbonate phase (Lyons et al., 2004; Present et al., 2015; Rennie and Turchyn, 2014).

Taking the isotopic data in the context of petrographic fabric, the maximum $\delta^{34}S$ composition of contemporaneous seawater sulfate is approximated by the lowest CAS $\delta^{34}S$ measurements, between 10‰ and 12‰ V-CDT. The lightest CAS measurements were consistently observed within dolomite debris-flow clasts

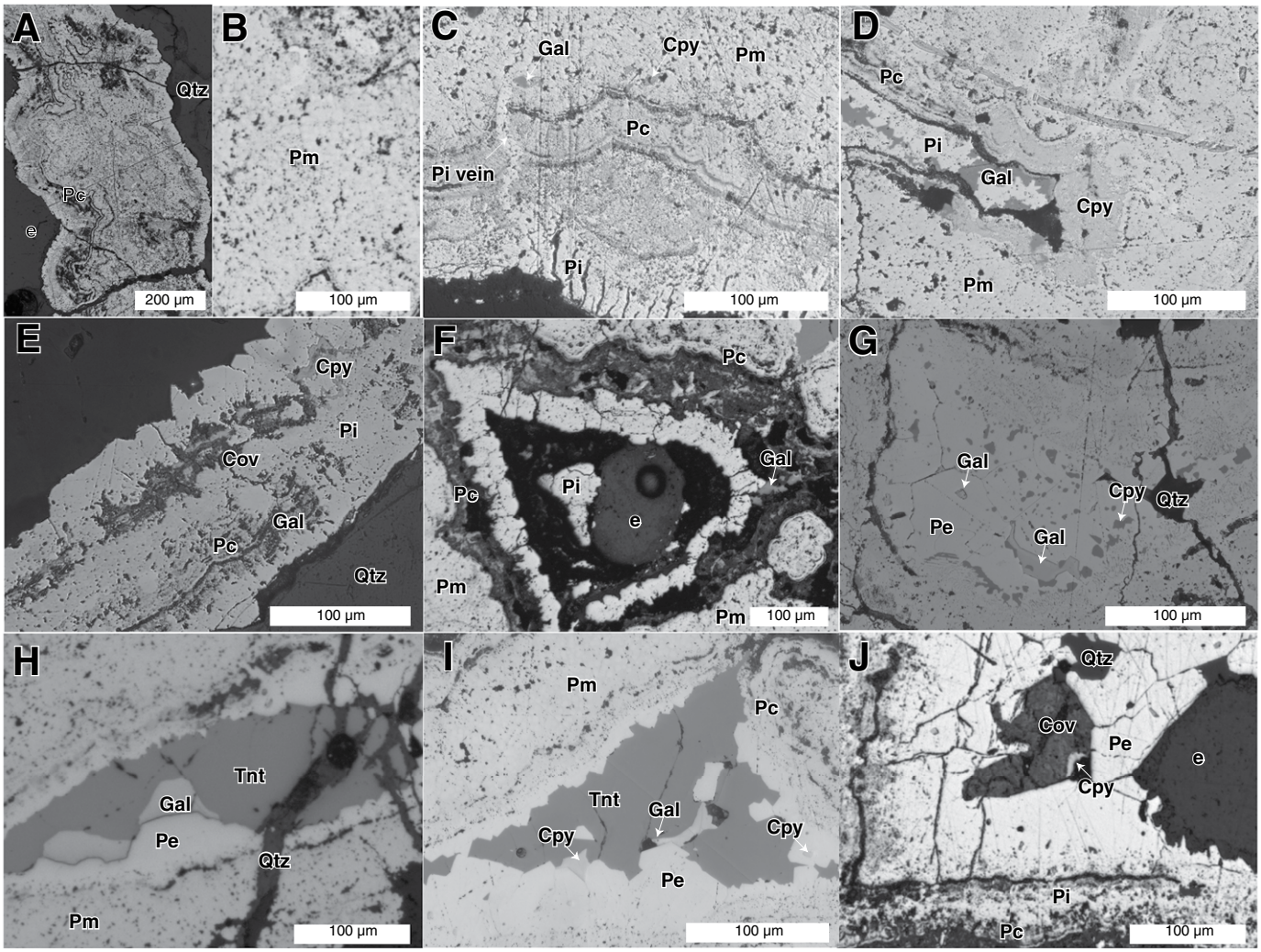

Figure 7. Reflected light photomicrographs from SC11-029–56.42 m showing sulfide minerals and textures associated with tube structures. Mineral texture abbreviations as in Table 2. (A) Colloform pyrite (Pc) comprises tube structures' walls, with growth direction into both void spaces; quartz (Qtz) fills void space to the right, and epoxy (e) used to mount the slide fills remnant porosity. (B) Mottled pyrite (Pm). (C) Intergrown colloform and mottled pyrite overgrown by irregular coarse pyrite (Pi) with anhedral blebs of galena (Gal) and chalcopyrite (Cpy). (D) Bands of colloform pyrite controlling overgrowth and replacement of mottled/colloform pyrite with chalcopyrite, and intergrowth of galena with irregular coarse pyrite. (E) Colloform pyrite overgrown by irregular coarse pyrite, galena, and chalcopyrite; the chalcopyrite is replaced by covellite (Cov). Quartz fills the tube structure. (F) Irregular coarse pyrite overgrowing colloform pyrite and filling porosity; galena replaces some colloform pyrite. (G) Euhedral coarse pyrite overgrowing colloform/mottled pyrite, with exsolved chalcopyrite and galena, cut by a quartz-filled fracture. (H) Tennantite (Tnt), galena, and euhedral coarse pyrite (Pe) fill porosity in mottled/colloform pyrite, cut by a quartz-filled fracture. (I) Chalcopyrite and galena intergrown with tennantite fill porosity remaining after euhedral coarse pyrite, with exsolved chalcopyrite and galena, overgrows mottled/colloform pyrite. (J) Covellite and chalcopyrite fill porosity remaining after euhedral coarse pyrite and irregular coarse pyrite overgrow colloform pyrite.

transported from outside the area of active sulfide mineralization, where closed-system sulfate reduction would be minimized due to less fixation by iron or less reduction by organic carbon (Jørgensen, 1979). An inferred seawater sulfate composition of 10‰–12‰ V-CDT is lighter than previously suggested on the basis of Newland Formation barites (Strauss, 1993; Strauss and Schieber, 1990; Zieg and Leitch, 1998), but it is comparable to previously reported CAS from the Newland Formation and other Mesoproterozoic successions (Gellatly and Lyons, 2005; Guo et al., 2015; Kah et al., 2004).

What we interpret as the paragenetically earliest pyrite (nodules in SC11-029–389.22 m; Fig. 8A; Supplemental Fig. DR4F [see footnote 1]) also has the lowest $\delta^{34}S$ composition (Table 4). Values as light as –18‰ V-CDT indicate fractionation from seawater sulfate of nearly 30‰ (Fig. 6E), comparable to kinetic fractionations associated with microbial sulfate reduction in an open system (Jørgensen, 1979). These data are generally lighter than in situ sulfur isotope data from Archean (i.e., before oxygenation of Earth's surface and therefore lower marine sulfate concentrations) diagenetic pyrite nodules, and they lack the isotopic zonation from core to rim that

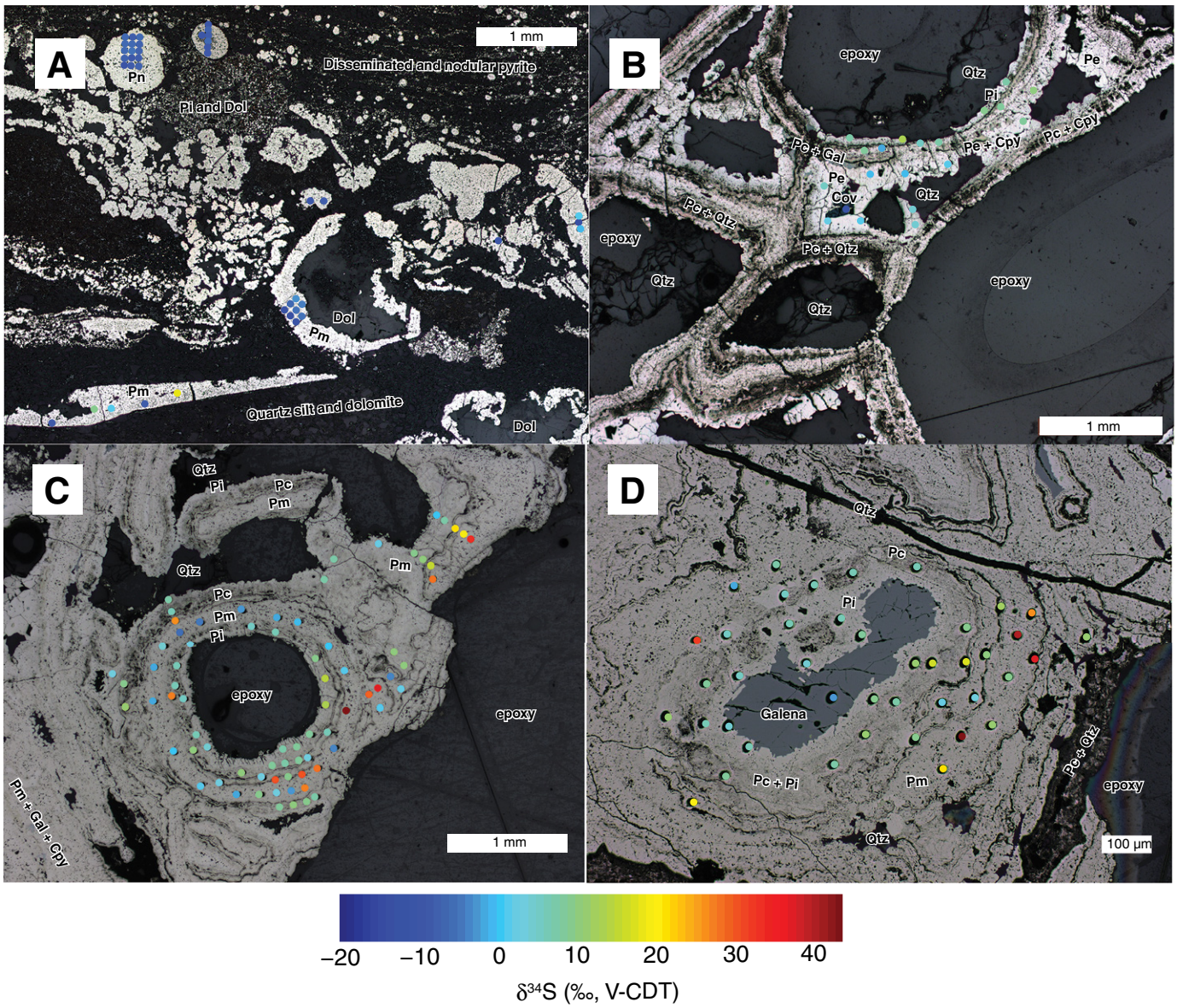

Figure 8. Secondary ion mass spectrometry (SIMS) sulfide-sulfur $\delta^{34}S$ analysis pits colored by isotopic composition overlain on plane-polarized reflected light composite photomicrographs. See Supplemental Figure DR2 (see text footnote 1) for location of sites on the thick sections. Further analysis pits are shown in Supplemental Figure DR4 (see text footnote 1). Mineral texture abbreviations are as in Table 2 (Qtz—quartz). (A) SC11-095–389.22 m, sites 7, 8, and 9. Pyrite nodules and fragments of tube structures in a thick conglomerate lamina within very thinly laminated striped shale. (B) SC11-029–56.42 m, site 6. Coarse pyrite overgrowing delicate pyrite-walled tube structures with partial quartz occlusion. (C) SC11-029–56.42 m, site 3. Pyrite-walled tube structures overgrown by coarse pyrite and largely devoid of porosity-occluding gangue minerals. (D) SC11-029–56.42 m, site 1. Pyrite-walled tube structure overgrown by coarse irregular pyrite and filled with galena, with a late quartz-filled fracture. V-CDT—Vienna-Canyon Diablo Troilite.

may have suggested more sulfate-limiting pore-fluid conditions during nodule growth (Fischer et al., 2014; Gregory et al., 2015; Johnson et al., 2013; Kamber and Whitehouse, 2007; Marin-Carbonne et al., 2014).

A broad range of isotopic compositions of early pyrite in the Helena Embayment was observed by Lyons et al. (2000) and Luepke and Lyons (2001) (Fig. 6D), who further noted large, systematic stratigraphic trends interpreted as basin-scale reservoir effects on the composition of pyrite. In contrast, Strauss and Schieber (1990) identified two phases in disseminated pyrite: a low $\delta^{34}S$ early diagenetic pyrite and a higher $\delta^{34}S$ coarsely crystalline concretionary overgrowth. They attributed the variability in pyrite compositions to changes in the diffusive supply of sulfate to the sediments, where heavier isotopic compositions reflected a more closed system (Jørgensen, 1979). With in situ measurements, we observed a pattern similar to that reported by Strauss and Schieber (1990), especially in SC11-029–389.22 m Site 5 (Supplemental Fig. DR4F [see footnote 1]). Early diagenetic nodules were found to be generally lighter than coarser pyrite overgrowths, consistent with minimal sulfate limitation during early pore-fluid

TABLE 3. SULFATE-SULFUR RESULTS

Sample	Type	% carbonate*	[CAS]† (ppm)	$\delta^{34}S_{SO4}$ (‰, V-CDT§)
Upper sulfide zone				
SC11-029, 49.09 m (a)	Barite lath	N.A.#	N.A.	18.32 ± 0.14**
SC11-029, 49.09 m (b)	Barite lath	N.A.	N.A.	16.22 ± 0.26
SC11-029, 61.185 m (a)	Dolomitic mudstone	88	656 ± 51	10.42 ± 0.61
SC11-029, 61.185 m (b)	Barite lath	N.A.	N.A.	14.15 ± 0.24
SC11-029, 61.185 m (c)	Barite lath	N.A.	N.A.	15.44 ± 0.57
SC11-095, 362.51 m (a)	Dolostone clast	79	152 ± 12	13.66 ± 1.00
SC11-095, 362.51 m (b)	Dolostone clast	55	217 ± 21	9.97 ± 1.09
SC11-095, 362.51 m (c)	Dolostone clast	61	129 ± 12	11.27 ± 0.82
SC11-095, 485.83 m (a)	Dolostone clast	91	23 ± 2	11.38 ± 1.50
SC11-095, 485.83 m (b)	Barite cement	N.A.	N.A.	15.40 ± 1.94
SC11-095, 486.29 m (a)	Barite lath	N.A.	N.A.	15.04 ± 0.21
SC11-095, 486.29 m (b)	Barite lath	N.A.	N.A.	17.64 ± 0.17
Middle sulfide zone				
SC10-06, 378.31 m	Dolostone clast	102††	70 ± 5	16.78 ± 0.98
Lower sulfide zone				
SC12-112, 335.02 m	Dolomitic mudstone	60	102 ± 9	25.45 ± 1.31
SC12-112, 327.83 m (a)	Dolomitic mudstone	51	334 ± 36	11.83 ± 0.64
SC12-112, 327.83 m (b)	Dolomitic mudstone	58	136 ± 13	14.78 ± 1.14
SC12-112, 372.83 m (c)	Dolomitic mudstone	53	388 ± 37	11.27 ± 0.82

*Functionally refers to the acid-soluble portion of the rock.
†ppm—parts per million by mass, equivalent to μg SO_4^{2-}/g carbonate.
§V-CDT—Vienna-Canyon Diablo Troilite reference standard.
#N.A.—not applicable.
**Uncertainties tabulated as 1σ standard error.
††Insoluble residue after dissolution too negligible to weigh accurately.

sulfate reduction and pyrite nodule growth. It is therefore likely that the pyrite nodules precipitated shallower in the sediments than the barite rosettes and coarse pyrite overgrowths, which show $\delta^{34}S$ enrichment suggesting pore-fluid sulfur isotope reservoir effects. Barium was likely supplied by the remineralization of organic matter in the sediments, and it was concentrated along diagenetic fronts at the base of the sulfate reduction zone (Torres et al., 1996).

Estimates for the concentration of sulfate in marine waters during the Mesoproterozoic range from <0.1 m*M* to 4.5 m*M* and may have been globally variable (Canfield et al., 2010; Kah et al., 2004; Luo et al., 2015; Sperling et al., 2014). The lowest estimates are based on observations of small isotopic differences (<10‰) between contemporaneous sulfate and sulfide (Canfield et al., 2010; Luo et al., 2015), and are precluded in the Helena Embayment by our data (Figs. 6B–6E) and other published data. In modern environments, Algeo et al. (2015) and Canfield et al. (2010) empirically identified a correlation between observed sulfur isotope fractionation and sulfate concentrations. If this relationship holds in the Mesoproterozoic, then the sulfur isotopic depletion we observed in the pyrite nodules—about 10‰–30‰ lighter than the $\delta^{34}S$ of contemporaneous seawater sulfate—correlates to 2–6 m*M* sulfate concentrations (with a mode of 3 m*M*) in the Helena Embayment during deposition of the Newland Formation (Algeo et al., 2015). This estimate is a conservative estimate of the minimum sulfate concentration, given the interpretation that seawater is represented by the lowest CAS $\delta^{34}S$ measurement and assuming that the pyrite nodules formed contemporaneously with the CAS.

TABLE 4. STATISTICAL DESCRIPTION OF SULFIDE $\delta^{34}S$ DATA

Mineral	n	Mean (‰)	1σ s.d.* (‰)	Median (‰)	IQR† (‰)
Pyrite texture					
Nodular pyrite (Pn)	61	–5.3	5.3	–5.5	4.4
Mottled pyrite (Pm)	108	10.3	12.5	7.5	17.2
Colloform pyrite (Pc)	63	10.8	7.1	9.2	4.6
Irregular coarse pyrite (Pi)	64	6.4	3.8	6.9	2.7
Euhedral coarse pyrite (Pe)	33	5.4	4.9	5.7	5.4
Coarse pyrite§	97	6.1	4.2	6.5	3.7
Base metal sulfides					
Chalcopyrite	5	3.9	1.2	3.4	1.6
Galena	6	–6.7#	1.2	–6.6#	2.2

*s.d.—standard deviation.
†IQR—interquartile range.
§Coarse pyrite is the joint population of Pi and Pe pyrite.
#No galena standard was used, so accuracy is unknown (but precision is reliable).

Precipitation of Tube Structures

While the pyrite-walled tube structures are interbedded with crinkly laminated pyrite and debris flows, intergrowth of mottled pyrite with colloform pyrite and quartz (Figs. 8B and 8D) suggests that, at least in some cases, they were closely associated with the early stages of base metal mineralization. We interpret that the tube structures formed at sites of hydrothermal fluid effluence to the seafloor (Fig. 9).

Fluid inclusion data indicate a moderate salinity (1.1–3.5 mol/kg) and a homogenization temperature of less than 250 °C for Black Butte hydrothermal fluids (Himes and Peterson, 1990); under these conditions, expelled fluids, upon mixing with cold seawater, would have acted as a brine denser than seawater (Himes and Peterson, 1990; Sangster, 2002). This would diminish the buoyancy of the expelled fluid relative to seawater, so precipitation and accretion patterns would resemble those at low-velocity modern diffuse vents (Hannington et al., 1995).

At diffuse hydrothermal vents, both biologic and inorganic processes contribute to the formation of tube-shaped structures. One possible biologic process would involve preservation of macroscopic organisms as a cast or mold. Preservation of macroscopic organisms (such as worm tubes) with broadly comparable size and porosity may have created similar structures in Phanerozoic deposits (e.g., Banks, 1985; Campbell et al., 2002; Haymon et al., 1984; Little et al., 1999a, 1999b; Moore et al., 1986), but there are few definitive examples of macroscopic organisms in Proterozoic strata and no known organisms that provide unambiguous analogs for tube formation. Although problematic macrofossils (*Grypania* and *Horodyskia*) have been described in shallower paleoenvironments in the Helena Embayment and other contemporaneous successions (Fedonkin and Yochelson, 2002; Kumar, 1995; Walter et al., 1990), these do not resemble known tube structures, and neither these nor any other Mesoproterozoic macrofossils have been described from the deep-slope, below-wave-base setting characteristic of Black Butte sedimentary rocks (Horodyski, 1993).

Alternatively, the tube structures' close association with crinkly laminated pyrite might suggest that they are unique Mesoproterozoic microbialites formed by the sulfide permineralization of microbial communities (McGoldrick and Zieg, 2004). Mineralization could have encrusted locally abundant mats or streamers of colonial or filamentous microorganisms, as is observed in cold seeps and alkaline springs (e.g., Arp et al., 1998; Barbieri and Cavalazzi, 2005; Cady et al., 2003; Fouke et al., 2000;

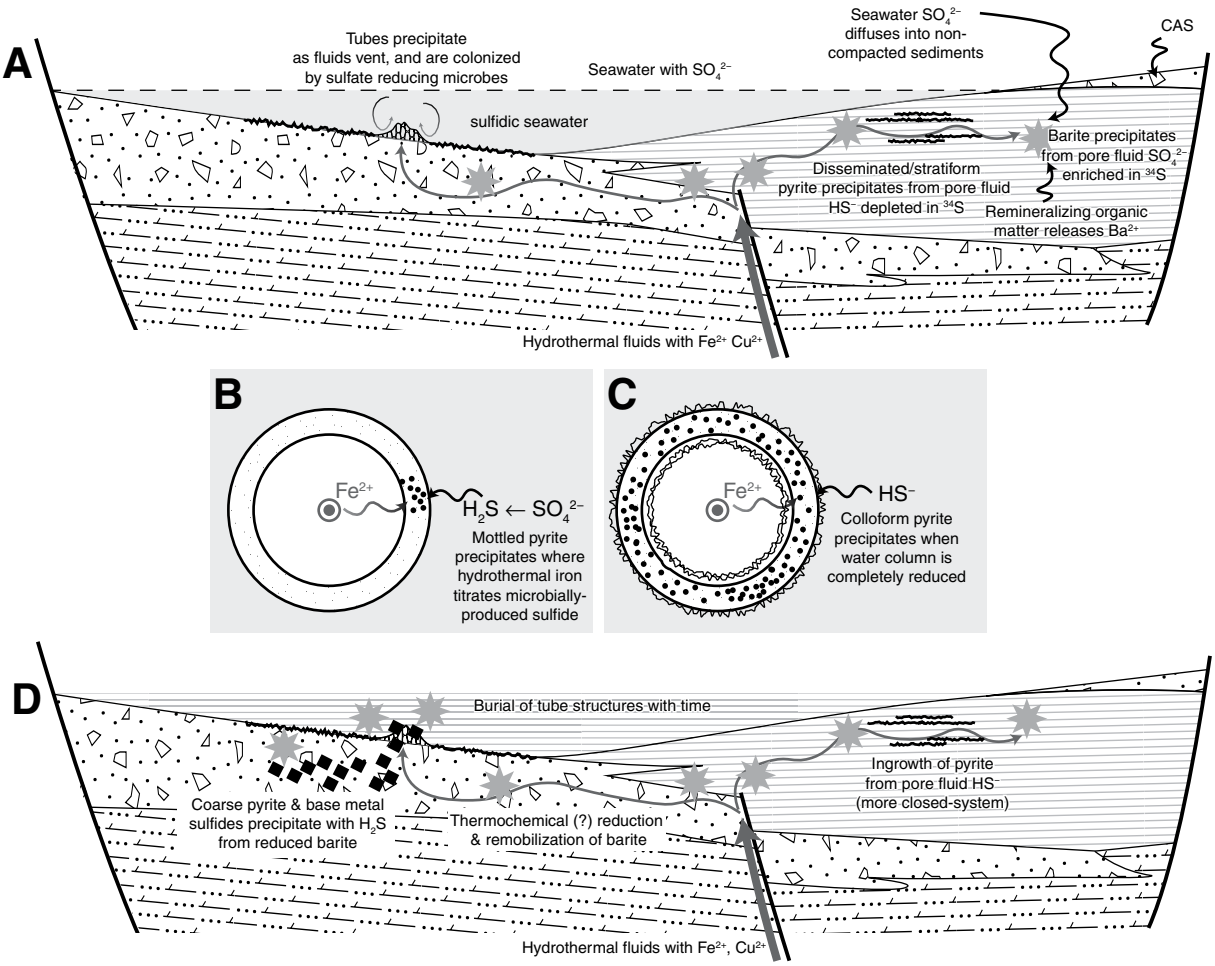

Figure 9. Schematic illustrating how seawater sulfate interacts with hydrothermal fluids to create tube-shaped vent structures of mottled and colloform pyrite. (A) Metalliferous hydrothermal fluids seep up, possibly along faults, and interact with seawater or diagenetically modified pore fluids. Disseminated and nodular pyrite forms from sulfide microbially produced in the sediments under open-system conditions with respect to seawater sulfate supply. Diagenetic barite precipitates deeper in the uncompacted sediments from residual pore-fluid sulfate isotopically distilled by microbial sulfate reduction and barium released by remineralizing organic matter. Tube-shaped conduits precipitate as the metalliferous fluids vent to the seafloor in the restricted basin, where euxinic or suboxic seawater contains temporally variable amounts of sulfate and sulfide. Possibly, microbial mats colonize the tube structures and seafloor near vent sites. (B–C) Cross section of a single tube-shaped fluid conduit. (B) Sulfide in the water column produced by microbial communities growing on or around the vent structures reacts with iron to precipitate mottled pyrite within the metastable precursor of the tube walls. (C) During intervals of nearly complete sulfate reduction in the basin, colloform pyrite precipitates on tube walls as iron is slowly supplied by continued venting. (D) After burial of the tube structures, continued supply of metals reacts with sulfate reduced from barite to form coarse pyrite and base metal sulfides. Fractionation of sulfur isotopes by thermochemical sulfate reduction of barite can explain the coarse pyrite and chalcopyrite isotopic compositions. Later coarse pyrite overgrowth of nodular and disseminated pyrite is also isotopically heavier than earlier pyrite, reflecting sulfur isotope distillation in the deeper pore fluids. CAS—carbonate-associated sulfate.

Hofmann and Farmer, 2000; Reitner et al., 2005). Biological accretion in this manner predicts a consistent three-dimensional form controlled by the morphology of microbial communities. Streamer fabrics are encapsulated in tube-shaped structures that have a near-constant diameter with a high aspect ratio controlled by the average colony size; aspect ratio and diameter have low variances. The strands are oriented roughly parallel to fluid flow or, in still water, under the influence of gravity (Cady et al., 2003; Hofmann and Farmer, 2000). Most sedimentary environments show fluid flow parallel to the sediment-water interface, which predicts that tube structures would have a strong preferential pore orientation in the horizontal plane.

The Black Butte tube structures have irregular shapes (Figs. 2 and 5G), not the consistent dimensions or repeating organization predicted by mineralization of macroscopic organisms. They do not have the high aspect ratio with

low variance, low variance of tube width, and strong horizontal preferred orientation (Table 1) predicted by mineralization of filamentous microbial communities by analogy to modern microbial hydrothermal communities. Thus, the three-dimensional form of the millimeter-scale tube structures does not match known biologic hydrothermal morphologies.

Encrustation of microbial material also predicts specific sulfide petrographic textures that are not observed in the Black Butte tube structures. Preservation of the microbial outline as a mold generally results from crystal precipitation toward a free aqueous surface (Jones et al., 2008; Li and Kusky, 2007; Shapiro and Fricke, 2002). However, colloform pyrite in the ~100 mm walls of the tube structures propagates away from both sides of the tube structures' walls (Figs. 8B and 8C), indicating a free surface on either side of the mottled pyrite. Perhaps organic material defining a millimeter-scale community structure was removed prior to colloform pyrite mineralization, but intergrowth of mottled and colloform pyrite (Fig. 8C) suggests that this is not the simplest option.

Abiotic mineralization at diffuse hydrothermal vents creates textures and structures similar to those found at Black Butte. Precipitation of early hydrothermal minerals governs fluid flow and controls redox and temperature gradients between hydrothermal fluids and seawater (Hannington et al., 1995; Tivey, 2007). The fluid conduits in these buildups have an internal architecture characterized by networks of millimeter-scale tortuous conduits similar to the Black Butte tube structures (Gamo et al., 1991; Kelley et al., 2001b; Koski et al., 1994; Ludwig et al., 2006). Tubes are highly variable in size and aspect ratio, with tube orientation generally in the direction of fluid flow, and often elongate normal to the sediment-water interface. Black Butte tube dimensions are similar to those in Lost City and Juan de Fuca networks, with mean dimensions for all samples within one standard deviation (Table 1; Haymon and Kastner, 1981; Kelley et al., 2001b). Further, the subvertical fabric, variably ovoid aspect ratio, millimeter-scale tortuous porosity, and extensive cementation in tube structures are consistent with morphologies found at modern diffuse vent sites (Delaney et al., 1992; Koski et al., 1994; Ludwig et al., 2006; Okumura et al., 2016).

By analogy to modern diffuse vent structures, mottled and colloform pyrite in the Black Butte tube structures probably replaced or precipitated on an unobserved earlier phase that defined the walls of the tube structures (Fig. 9A). As iron-rich hydrothermal fluid diffused through these walls and met sulfide in seawater, granular sulfides would have precipitated within the precursor (Fig. 9B; Haymon, 1983; Tivey, 1995). The replaced initial tube walls were likely iron-sulfide colloids or poorly ordered minerals (Russell and Hall, 1997; Russell et al., 1989), but various metastable phases (e.g., anhydrite, brucite, aragonite) commonly precipitate at deep vent sites and do not remain in the geologic record (Breier et al., 2010; Haymon and Kastner, 1981; Kelley et al., 2001b; Ludwig et al., 2006; Okumura et al., 2016).

Overall, the texture and three-dimensional structure are difficult to explain as bioconstructions without hypothesizing a complicated and entirely new model for microbial communities. Nonetheless, the low and variable $\delta^{34}S$ composition of the mottled pyrite suggests microbial sulfate reduction contributed much of the sulfide. Mottled pyrite has an extremely variable sulfur isotopic composition (Interquartile Range [IQR] = 17.2‰; Table 4) over millimeter scales, with compositions as light as –20‰ V-CDT and as heavy at 45‰ V-CDT (Fig. 6F). We suggest, then, that the three-dimensional features of the tube structures primarily reflect fluid flow, whereas sulfur geochemistry indicates that sulfate-reducing bacteria provided sulfide for the accreting structures. Colonization of vent structures is common at modern vents. For example, at the modern Lost City and Shinkai Seep hydrothermal deposits, microbial consortia colonize intricate tube-shaped, 100 µm to millimeter-scale pores in aragonite-brucite buildups (Kelley et al., 2005; Okumura et al., 2016). There is evidence of encrustation of some filamentous micron-scale organisms. However, the dominant (>1 mm) porosity structure is governed by the diffuse fluid-flow regime (Kelley et al., 2005; Ludwig et al., 2006; Okumura et al., 2016; Schrenk et al., 2004). The chemical gradients at the vent site, combined with a complicated porosity structure, allow microbial communities to take hold. It is not clear how extensive of a role the microbial community plays in nucleating minerals or modifying fluid flow to shape the large fluid conduits (Emerson and Moyer, 2002; Steen et al., 2016). A chemoautotrophic community—in this case, microbial sulfate reducers—likely colonized vents and increased the redox gradient to allow metal deposition during the Mesoproterozoic at Black Butte (Fig. 9B).

In some cases, coarse marcasite overgrows the mottled and colloform pyrite in the tube structures (Fig. 2D). Marcasite is a metastable polymorph of pyrite that forms below about pH 4 (Murowchick and Barnes, 1986), mostly likely from the oxidation of hydrogen sulfide on a colloidal precursor (Schoonen and Barnes, 1991). Perhaps some vents had sulfide-oxidizing microbes colonizing the vent, allowing local lowering of pH in the microbial community and promoting marcasite deposition (Juniper et al., 1992; Schieber, 2011; White et al., 2013). If so, the depositional basin of the Newland Formation was at least episodically and transiently oxic.

Despite its intergrowth with mottled pyrite, the sulfur isotopic composition of colloform pyrite is much less variable (IQR = 4.5‰), and it is heavier (Figs. 6F and 6G); the median value (9.2‰ V-CDT) is similar to the inferred composition of contemporaneous seawater sulfate. Colloform pyrite is also intimately associated with quartz (Figs. 8B, 8C, and 8D), and it has an isotopic composition similar to later base metal minerals (Fig. 6G). The colloform texture is associated with precipitation into open space at rates controlled by reactant supply (Anderson et al., 1998; Koski et al., 1994), and its isotopic composition is consistent with quantitative reduction of seawater sulfate. If seawater in the Helena Embayment were completely reduced, the isotopic composition of the sulfide would match that of seawater sulfate, and microbial sulfate-reducing communities would be less active. Complete reduction of seawater sulfate at the vent site would favor pyrite precipitation governed by iron supply from the vent, producing the colloform texture (Fig. 9C). Resupply of sulfate to the water column by mixing or diffusion into the deep basin would lead to a rejuvenation of the microbial sulfate-reducing community and renewed mottled pyrite deposition with variable isotopic composition.

Base Metal Mineralization

The mottled and colloform pyrite comprising the tube structures is overgrown by coarse pyrite, galena, and cupriferous minerals (Figs. 6A and 7), likely after burial of the structures (Graham et al., 2012; White et al., 2013). Graham et al. (2012) suggested that later mineralizing fluids at Black Butte were hotter or more oxidizing, allowing replacement of barite and transport of copper. The isotopic compositions of irregular and euhedral coarse pyrite are slightly depleted from contemporaneous seawater sulfate (mean $\delta^{34}S$ = 6.1‰; Table 4). Our limited analyses of chalcopyrite (mean $\delta^{34}S$ = 3.9‰) are heavier than the mottled pyrite and lighter than seawater sulfate, and consistent with data reported by Zieg and Leitch (1998; –5.1‰–7.1‰; Fig. 6J). The coarse pyrite and base metal sulfides paragenetically follow the massive barite that fills the pyrite-walled tube structures, which is isotopically similar to the early diagenetic bladed barite (Fig. 6B; Gellatly and Lyons, 2005; Strauss, 1993; Strauss and Schieber, 1990; Zieg and Leitch, 1998).

Other sediment-hosted sulfide deposits similarly display two sulfur sources: a light and

variable source interpreted as a biogenic result of microbial sulfate reduction, and a heavier and more homogeneous source interpreted as leached from underlying rock units (Anderson et al., 1998; Blakeman et al., 2002; Eldridge et al., 1993; Ireland et al., 2004). While sulfide-rich fluids will easily transport barium, they should not transport significant copper unless they are hotter than ~250 °C (Cooke et al., 2000; Hitzman et al., 2010; Xiao et al., 1998). Zieg and Leitch (1998) reported a vein chalcopyrite-pyrite equilibrium temperature of 276 °C. White et al. (2013) calculated lower deposition temperatures (<225 °C) from the equilibrium stability of more minor cobalt-, nickel-, and zinc-bearing minerals, although variability in the composition of some minerals may allow for temperatures up to ~300 °C. Therefore, if sulfidic, the hydrothermal fluids must have been between 250 °C and 300 °C, and deposition occurred by cooling to less than ~225 °C. However, such temperatures are close to the saturation of cupriferous minerals (Xiao et al., 1998), predicting the formation of a significant mineralized feeder zone below sites of hydrothermal effluence (Cooke et al., 2000; Goodfellow et al., 1993; Large et al., 2005; Leach et al., 2005), which is not well developed at Black Butte.

Instead, the presumed source for the base metals is the hematitic Neihart Formation (White et al., 2013; Zieg et al., 2013), which would have buffered any sulfur in the hydrothermal fluids to a sulfate-rich speciation that could not transport barium. Like the earlier mottled and colloform pyrite, coarse pyrite and base metal sulfides would have deposited upon meeting a reservoir of sulfide produced by sulfate reduction (Fig. 9D). However, the latter phases would have precipitated deeper in the hydrothermal system (Dixon and Davidson, 1996; Gadd et al., 2017; Ireland et al., 2004; Large et al., 1998), where reduction of preexisting early diagenetic barite may have provided sulfide for the coarse pyrite and base metal sulfides. The sulfur isotopic composition of barite, coarse pyrite, and base metal sulfides is consistent with thermal reduction, which would have produced sulfide that was 10‰–20‰ lower in $\delta^{34}S$ than the barite (Figs. 6B, 6C, and 6H–6J; Johnson et al., 2004; Kelley et al., 2004; Powell and Macqueen, 1984). Barium liberated from the reduction of early diagenetic barite would migrate up toward the base of the microbial sulfate-reduction zone, creating a barite front in the hydrothermal system, as observed in modern and Phanerozoic hydrothermal barite deposits (Eickmann et al., 2014; Johnson et al., 2009). Addition of more sulfate migrating with the metalliferous fluids could also promote reprecipitation of barite, as observed in modern continental slope sediments (Feng and Roberts, 2011; Torres et al., 1996). While the sulfur isotopic composition of sulfate migrating with the metalliferous fluids at Black Butte is unknown, future examination of the oxygen isotopic composition and high-precision measurement of all four stable sulfur isotopes may discern between these barite precipitation mechanisms (Feng and Roberts, 2011).

The relative transport rates of metalliferous brines and sulfur over the life of a long-lived hydrothermal system may vary dramatically. Increasing temperatures at the trap site and temporally variable fluid circulation could remobilize and isotopically homogenize the sulfide minerals. Such remobilization of sulfides by later, hotter fluids was invoked by Graham et al. (2012) to explain the unusual occurrence of chalcopyrite inclusions in barite. Temporally variable transport of metals and sulfur results in variable redox conditions at the site of deposition, indicated by barite codepositing or alternating paragenetically with sulfides (Graham et al., 2012; Huston et al., 2007; Samson and Russell, 1987).

SUMMARY AND CONCLUSIONS

Tube structures at the sediment-hosted Black Butte Copper Mine Project deposit are millimeter-scale porous networks of mottled and colloform pyrite that are overgrown by base metal sulfides. These structures precipitated at sites of diffuse hydrothermal venting by means of abiotic processes broadly similar to those observed in modern hydrothermal seeps, thereby documenting the direct interaction of hydrothermal fluids with seawater. We suggest that pyrite in tube walls represents syngenetic mineralization of tube-shaped fluid conduits, the shape of which was determined by low-buoyancy venting of the hydrothermal fluids. Mottled pyrite replaced an initial conduit composed of a metastable iron-sulfur colloid, carbonate, or hydroxide. During temporary periods of complete water-column sulfate reduction, colloform pyrite overgrew the tube structures. After burial, the tube structures were overgrown by coarse pyrite, base metal sulfides, barite, and quartz or dolomite.

The tube structures formed in environments that had extensive diagenetic pyrite and barite precipitation, ultimately derived from seawater that had concentrations of sulfate ~2–6 m*M* or greater. The isotopic compositions of these minerals were controlled by kinetic effects associated with microbial sulfate reduction in sediments that left residual sulfate isotopically ^{34}S-enriched with respect to seawater sulfate. During deposition of the lower Newland Formation, we estimate that the $\delta^{34}S$ of seawater sulfate in the Helena Embayment was ~10‰ enriched in ^{34}S relative to V-CDT.

The mineralogy and sulfur isotopic composition of the tube structures suggest that bottom waters in the Helena Embayment during deposition of the Newland Formation may have had quite variable redox conditions. Large sulfur isotopic variation of mottled pyrite suggests sulfate-rich seawater was being actively reduced under varying degrees of sulfate limitation. A more homogeneous composition for the intergrown colloform pyrite suggests that, occasionally, much of the bottom-water sulfate was reduced to sulfide. Finally, precipitation of marcasite, possible only under locally acidic conditions, suggests that some intervals were oxic, allowing sulfur-oxidizing communities to colonize the vents and seafloor. Base metal mineralization occurred deeper in the hydrothermal system, and deposition occurred by titration with sulfide derived from reductive remobilization of barite.

The recognition of diffuse hydrothermal vents in a sediment-hosted deposit provides a rare opportunity to examine the interactions among hydrothermal fluids, seawater, and benthic microbiota in Mesoproterozoic oceans. The close association with crinkly laminated pyrite suggests there may have been extensive microbial sulfate-reducing communities associated with vent sites. The particularly large sulfur isotopic range of mottled pyrite suggests, like in modern and fossilized diffuse vents, that the chimneys may have been colonized by sulfate reducers as well. It is unclear what role, besides providing sulfide to titrate the metals, the microbes played in modifying tube structure, fluid flow, or mineralogy. However, the dominant porosity structure of the tube structures reflects the diffuse effluence of buoyant fluids to the seafloor.

ACKNOWLEDGMENTS

This project originated during the Agouron Institute Advanced Field Course during July 2013. Funding was provided by the Agouron Institute and the National Aeronautics and Space Administration (NASA) Astrobiology Institute (NAI). We thank Tintina Resources, Inc., especially Chance Matthews, for access to drill core and outcrop associated with the Black Butte Copper Project. We also thank Tyler Mackey, James Wray, Ross Williams, Ken Williford, and Doug Archer for thoughtful discussion and field assistance, and especially Kirsten Siebach for excellent photos. We thank Peter Girguis and Roger Summons for samples of modern hydrothermal vents used in the micro–computed tomography analyses; Jess Adkins, Nathan Dalleska, Yunbin Guan, Jena Johnson, Guillaume Paris, and Jason Price for analytical support; and Michael Russell for help interpreting our data. We thank Peter McGoldrick, Garth Graham, and an additional anonymous reviewer for helpful and thoughtful reviews that greatly improved this submission. We thank the Editors Aaron Cavosie and Fernando Corfu for their help managing and preparing this manuscript.

REFERENCES CITED

Aleinikoff, J.N., Lund, K., and Fanning, C.M., 2015, SHRIMP U-Pb and REE data pertaining to the origins of xenotime in Belt Supergroup rocks: Evidence for ages of deposition, hydrothermal alteration, and metamorphism: Canadian Journal of Earth Sciences, v. 52, p. 722–745, doi:10.1139/cjes-2014-0239.

Algeo, T., Luo, G., Song, H., Lyons, T., and Canfield, D., 2015, Reconstruction of secular variation in seawater sulfate concentrations: Biogeosciences, v. 12, no. 7, p. 2131–2151, doi:10.5194/bg-12-2131-2015.

Anderson, I.K., Ashton, J.H., Boyce, A.J., Fallick, A.E., and Russell, M.J., 1998, Ore depositional process in the Navan Zn-Pb deposit, Ireland: Economic Geology and the Bulletin of the Society of Economic Geologists, v. 93, no. 5, p. 535–563, doi:10.2113/gsecongeo.93.5.535.

Arp, G., Hofmann, J., and Reitner, J., 1998, Microbial fabric formation in spring mounds ("microbialites") of alkaline salt lakes in the Badain Jaran Sand Sea, PR China: Palaios, v. 13, no. 6, p. 581–592, doi:10.2307/3515349.

Banks, D.A., 1985, A fossil hydrothermal worm assemblage from the Tynagh lead–zinc deposit in Ireland: Nature, v. 313, p. 128–131, doi:10.1038/313128a0.

Barbieri, R., and Cavalazzi, B., 2005, Microbial fabrics from Neogene cold seep carbonates, Northern Apennine, Italy: Palaeogeography, Palaeoclimatology, Palaeoecology, v. 227, no. 1-3, p. 143–155, doi:10.1016/j.palaeo.2005.04.026.

Blakeman, R.J., Ashton, J.H., Boyce, A.J., Fallick, A.E., and Russell, M.J., 2002, Timing of interplay between hydrothermal and surface fluids in the Navan Zn + Pb orebody, Ireland: Evidence from metal distribution trends, mineral textures, and $\delta^{34}S$ analyses: Economic Geology and the Bulletin of the Society of Economic Geologists, v. 97, no. 1, p. 73–91, doi:10.2113/gsecongeo.97.1.73.

Boyce, A., Coleman, M., and Russell, M., 1983, Formation of fossil hydrothermal chimneys and mounds from Silvermines, Ireland: Nature, v. 306, no. 5943, p. 545–550, doi:10.1038/306545a0.

Boyce, A.J., Little, C.T.S., and Russell, M.J., 2003, A new fossil vent biota in the Ballynoe barite deposit, Silvermines, Ireland: Evidence for intracratonic sea-floor hydrothermal activity about 352 Ma: Economic Geology and the Bulletin of the Society of Economic Geologists, v. 98, no. 3, p. 649–656.

Bradley, A.S., 2009, Organic Geochemical Biosignatures in Alkaline Hydrothermal Systems [Ph.D. thesis]: Cambridge, Massachusetts, Massachusetts Institute of Technology, 269 p.

Bradley, A.S., Hayes, J.M., and Summons, R.E., 2009, Extraordinary ^{13}C enrichment of diether lipids at the Lost City Hydrothermal Field indicates a carbon-limited ecosystem: Geochimica et Cosmochimica Acta, v. 73, no. 1, p. 102–118, doi:10.1016/j.gca.2008.10.005.

Breier, J.A., White, S.N., and German, C.R., 2010, Mineral–microbe interactions in deep-sea hydrothermal systems: A challenge for Raman spectroscopy: Philosophical Transactions of the Royal Society, ser. A, Mathematical, Physical and Engineering Sciences, v. 368, no. 1922, p. 3067.

Breit, G.N., Simmons, E.C., and Goldhaber, M.B., 1985, Dissolution of barite for the analysis of strontium isotopes and other chemical and isotopic variations using aqueous sodium carbonate: Chemical Geology–Isotope Geoscience Section, v. 52, no. 3-4, p. 333–336, doi:10.1016/0168-9622(85)90043-0.

Burdett, J.W., Arthur, M.A., and Richardson, M., 1989, A Neogene seawater sulfur isotope age curve from calcareous pelagic microfossils: Earth and Planetary Science Letters, v. 94, p. 189–198, doi:10.1016/0012-821X(89)90138-6.

Cady, S.L., Farmer, J.D., Grotzinger, J.P., Schopf, J.W., and Steele, A., 2003, Morphological biosignatures and the search for life on Mars: Astrobiology, v. 3, no. 2, p. 351–368, doi:10.1089/153110703769016442.

Campbell, K.A., Farmer, J.D., and Des Marais, D., 2002, Ancient hydrocarbon seeps from the Mesozoic convergent margin of California: Carbonate geochemistry, fluids and palaeoenvironments: Geofluids, v. 2, no. 2, p. 63–94, doi:10.1046/j.1468-8123.2002.00022.x.

Canfield, D.E., Farquhar, J., and Zerkle, A.L., 2010, High isotope fractionations during sulfate reduction in a low-sulfate euxinic ocean analog: Geology, v. 38, no. 5, p. 415–418, doi:10.1130/G30723.1.

Cooke, D.R., Bull, S.W., Large, R.R., and McGoldrick, P.J., 2000, The importance of oxidized brines for the formation of Australian Proterozoic stratiform sediment-hosted Pb-Zn (Sedex) deposits: Economic Geology and the Bulletin of the Society of Economic Geologists, v. 95, no. 1, p. 1–18, doi:10.2113/gsecongeo.95.1.1.

Delaney, J.R., Robigou, V., McDuff, R.E., and Tivey, M.K., 1992, Geology of a vigorous hydrothermal system on the Endeavour Segment, Juan de Fuca Ridge: Journal of Geophysical Research–Solid Earth, v. 97, no. B13, p. 19,663–19,682, doi:10.1029/92JB00174.

Dixon, G., and Davidson, G.J., 1996, Stable isotope evidence for thermochemical sulfate reduction in the Dugald River (Australia) strata-bound shale-hosted zinc–lead deposit: Chemical Geology, v. 129, no. 3-4, p. 227–246, doi:10.1016/0009-2541(95)00177-8.

Dunster, J.N., 1997, The Lady Loretta Formation: Sedimentology and Stratiform Sediment-Hosted Base Metal Mineralisation (2 volumes) [Ph.D. thesis]: Hobart, Tasmania, Australia, University of Tasmania, 386 p.

Eickmann, B., Thorseth, I.H., Peters, M., Strauss, H., Bröcker, M., and Pedersen, R.B., 2014, Barite in hydrothermal environments as a recorder of subseafloor processes: A multiple-isotope study from the Loki's Castle vent field: Geobiology, v. 12, no. 4, p. 308–321, doi:10.1111/gbi.12086.

Eldridge, C.S., Williams, N., and Walshe, J.L., 1993, Sulfur isotope variability in sediment-hosted massive sulfide deposits as determined using the ion microprobe SHRIMP: II. A study of the H.Y.C. Deposit at McArthur River, Northern Territory, Australia: Economic Geology and the Bulletin of the Society of Economic Geologists, v. 88, p. 1–26, doi:10.2113/gsecongeo.88.1.1.

Emerson, D., and Moyer, C.L., 2002, Neutrophilic Fe-oxidizing bacteria are abundant at the Loihi Seamount hydrothermal vents and play a major role in Fe oxide deposition: Applied and Environmental Microbiology, v. 68, no. 6, p. 3085–3093, doi:10.1128/AEM.68.6.3085-3093.2002.

Farquhar, J., Wu, N., Canfield, D.E., and Oduro, H., 2010, Connections between sulfur cycle evolution, sulfur isotopes, sediments, and base metal sulfide deposits: Economic Geology and the Bulletin of the Society of Economic Geologists, v. 105, no. 3, p. 509–533, doi:10.2113/gsecongeo.105.3.509.

Fedonkin, M.A., and Yochelson, E.L., 2002, Middle Proterozoic (1.5 Ga) *Horodyskia moniliformis* Yochelson and Fedonkin, the oldest known tissue-grade colonial eucaryote: Smithsonian Contributions to Paleobiology, v. 94, p. 1–29.

Feng, D., and Roberts, H.H., 2011, Geochemical characteristics of the barite deposits at cold seeps from the northern Gulf of Mexico continental slope: Earth and Planetary Science Letters, v. 309, no. 1-2, p. 89–99.

Fischer, W.W., Fike, D.A., Johnson, J.E., Raub, T.D., Guan, Y., Kirschvink, J.L., and Eiler, J.M., 2014, SQUID–SIMS is a useful approach to uncover primary signals in the Archean sulfur cycle: Proceedings of the National Academy of Sciences, v. 111, p. 5468–5473.

Fouke, B.W., Farmer, J.D., Des Marais, D.J., Pratt, L., Sturchio, N.C., Burns, P.C., and Discipulo, M.K., 2000, Depositional facies and aqueous-solid geochemistry of travertine-depositing hot springs (Angel Terrace, Mammoth Hot Springs, Yellowstone National Park, U.S.A.): Journal of Sedimentary Research, v. 70, no. 3, p. 565–585, doi:10.1306/2DC40929-0E47-11D7-8643000102C1865D.

Früh-Green, G.L., Kelley, D.S., Bernasconi, S.M., Karson, J.A., Ludwig, K.A., Butterfield, D.A., Boschi, C., and Proskurowski, G., 2003, 30,000 years of hydrothermal activity at the Lost City Vent Field: Science, v. 301, no. 5632, p. 495–498, doi:10.1126/science.1085582.

Gadd, M.G., Layton-Matthews, D., Peter, J.M., Paradis, S., and Jonasson, I.R., 2016, The world-class Howard's Pass SEDEX Zn-Pb district, Selwyn Basin, Yukon. Part II: The roles of thermochemical and bacterial sulfate reduction in metal fixation: Mineralium Deposita, v. 52, p. 405–419, doi:10.1007/s00126-016-0672-x.

Gamo, T., Sakai, H., Kim, E.-S., Shitashima, K., and Ishibashi, J.-I., 1991, High alkalinity due to sulfate reduction in the CLAM hydrothermal field, Okinawa Trough: Earth and Planetary Science Letters, v. 107, no. 2, p. 328–338, doi:10.1016/0012-821X(91)90080-2.

Gellatly, A.M., and Lyons, T.W., 2005, Trace sulfate in mid-Proterozoic carbonates and the sulfur isotope record of biospheric evolution: Geochimica et Cosmochimica Acta, v. 69, p. 3813–3829, doi:10.1016/j.gca.2005.01.019.

Glickson, D.A., Kelley, D.S., and Delaney, J.R., 2007, Geology and hydrothermal evolution of the Mothra Hydrothermal Field, Endeavour Segment, Juan de Fuca Ridge: Geochemistry Geophysics Geosystems, v. 8, no. 6, Q06010, doi:10.1029/2007GC001588.

Godlewski, D., and Zieg, G., 1984, Stratigraphy and depositional setting of the Precambrian Newland Limestone, *in* Hobbs, S.W., ed., The Belt, Abstracts and Summaries Belt Symposium II, 1983: Montana Bureau of Mines and Geology Special Publication 90, p. 2–4.

Goodfellow, W., Lydon, J., and Turner, R., 1993, Geology and genesis of stratiform sediment-hosted (SEDEX) zinc-lead-silver sulphide deposits, *in* Kirkham, R.V., Sinclair, W.D., Thorpe, R.I., and Duke, J.M., eds., Mineral Deposit Modeling: Geological Association of Canada Special Paper 40, p. 201–251.

Graham, G., Hitzman, M.W., and Zieg, J., 2012, Geologic setting, sedimentary architecture, and paragenesis of the Mesoproterozoic sediment-hosted Sheep Creek Cu-Co-Ag deposit, Helena Embayment, Montana: Economic Geology and the Bulletin of the Society of Economic Geologists, v. 107, no. 6, p. 1115–1141, doi:10.2113/econgeo.107.6.1115.

Gregory, D.D., Large, R.R., Halpin, J.A., Steadman, J.A., Hickman, A.H., Ireland, T.R., and Holden, P., 2015, The chemical conditions of the late Archean Hamersley Basin inferred from whole rock and pyrite geochemistry with $\Delta^{33}S$ and $\delta^{34}S$ isotope analyses: Geochimica et Cosmochimica Acta, v. 149, p. 223–250, doi:10.1016/j.gca.2014.10.023.

Grotzinger, J.P., and Knoll, A.H., 1999, Stromatolites in Precambrian carbonates: Evolutionary mileposts or environmental dipsticks?: Annual Review of Earth and Planetary Sciences, v. 27, no. 1, p. 313–358, doi:10.1146/annurev.earth.27.1.313.

Guo, H., Du, Y., Kah, L.C., Hu, C., Huang, J., Huang, H., Yu, W., and Song, H., 2015, Sulfur isotope composition of carbonate-associated sulfate from the Mesoproterozoic Jixian Group, North China: Implications for the marine sulfur cycle: Precambrian Research, v. 266, p. 319–336, doi:10.1016/j.precamres.2015.05.032.

Hannington, M.D., Jonasson, I.R., Herzig, P.M., and Petersen, S., 1995, Physical and chemical processes of seafloor mineralization at mid-ocean ridges, *in* Humphris, S.E., Zierenberg, R.A., Mullineaux, L.S., and Thomson, R.E., eds., Seafloor Hydrothermal Systems: Physical, Chemical, Biological, and Geological Interactions: American Geophysical Union Geophysical Monograph 91, p. 115–157, doi:10.1029/GM091p0115.

Haymon, R.M., 1983, Growth history of hydrothermal black smoker chimneys: Nature, v. 301, no. 5902, p. 695–698, doi:10.1038/301695a0.

Haymon, R.M., and Kastner, M., 1981, Hot spring deposits on the East Pacific Rise at 21°N: Preliminary description of mineralogy and genesis: Earth and Planetary Science Letters, v. 53, no. 3, p. 363–381, doi:10.1016/0012-821X(81)90041-8.

Haymon, R.M., Koski, R.A., and Sinclair, C., 1984, Fossils of hydrothermal vent worms from Cretaceous sulfide ores of the Samail ophiolite, Oman: Science, v. 223, no. 4643, p. 1407–1409, doi:10.1126/science.223.4643.1407.

Himes, M., and Peterson, E., 1990, Geological and mineralogical characteristics of the Sheep Creek copper-cobalt sediment-hosted stratabound sulfide deposit, Meagher County, Montana, *in* Hausen, D., Halbe, D., Peterson, E., and Tafuri, W., eds., Gold '90; Proceedings of the Gold '90 Symposium, Salt Lake City, Utah, February 26 to March 1, 1990: Littleton, Colorado, Society for Mining, Metallurgy, and Exploration, Inc., p. 533–546.

Hitzman, M.W., Selley, D., and Bull, S., 2010, Formation of sedimentary rock–hosted stratiform copper deposits

through Earth history: Economic Geology and the Bulletin of the Society of Economic Geologists, v. 105, no. 3, p. 627–639, doi:10.2113/gsecongeo.105.3.627.

Hofmann, B.A., and Farmer, J.D., 2000, Filamentous fabrics in low-temperature mineral assemblages: Are they fossil biomarkers? Implications for the search for a subsurface fossil record on the early Earth and Mars: Planetary and Space Science, v. 48, no. 11, p. 1077–1086, doi:10.1016/S0032-0633(00)00081-7.

Horodyski, R.J., 1993, Paleontology of Proterozoic shales and mudstones: Examples from the Belt Supergroup, Chuar Group and Pahrump Group, western USA: Precambrian Research, v. 61, no. 3-4, p. 241–278, doi:10.1016/0301-9268(93)90116-J.

Huston, D.L., Maas, R., and Czarnota, K., 2007, The Age and Genesis of the Nifty Copper Deposit: Back to the Future: Canberra, Australia, Geoscience Australia Professional Opinion, 2007/03, 22 p.

Ireland, T., Large, R. R., McGoldrick, P., and Blake, M., 2004, Spatial distribution patterns of sulfur isotopes, nodular carbonate, and ore textures in the McArthur River (HYC) Zn-Pb-Ag deposit, Northern Territory, Australia: Economic Geology and the Bulletin of the Society of Economic Geologists, v. 99, no. 8, p. 1687–1709.

Johnson, C.A., Kelley, K.D., and Leach, D.L., 2004, Sulfur and oxygen isotopes in barite deposits of the western Brooks Range, Alaska, and implications for the origin of the Red Dog massive sulfide deposits: Economic Geology and the Bulletin of the Society of Economic Geologists, v. 99, no. 7, p. 1435–1448, doi:10.2113/gsecongeo.99.7.1435.

Johnson, C.A., Emsbo, P., Poole, F.G., and Rye, R.O., 2009, Sulfur- and oxygen-isotopes in sediment-hosted stratiform barite deposits: Geochimica et Cosmochimica Acta, v. 73, no. 1, p. 133–147, doi:10.1016/j.gca.2008.10.011.

Johnson, J.E., Webb, S.M., Thomas, K., Ono, S., Kirschvink, J.L., and Fischer, W.W., 2013, Manganese-oxidizing photosynthesis before the rise of cyanobacteria: Proceedings of the National Academy of Sciences of the United States of America, v. 110, no. 28, p. 11,238–11,243.

Jones, B., de Ronde, C.E.J., and Renaut, R.W., 2008, Mineralized microbes from Giggenbach submarine volcano: Journal of Geophysical Research–Solid Earth, v. 113, no. B8, p. B08S05, doi:10.1029/2007JB005482.

Jørgensen, B.B., 1979, A theoretical model of the stable sulfur isotope distribution in marine sediments: Geochimica et Cosmochimica Acta, v. 43, p. 363–374, doi:10.1016/0016-7037(79)90201-1.

Juniper, S.K., Jonasson, I.R., Tunnicliffe, V., and Southward, A.J., 1992, Influence of a tube-building polychaete on hydrothermal chimney mineralization: Geology, v. 20, no. 10, p. 895–898, doi:10.1130/0091-7613(1992)020<0895:IOATBP>2.3.CO;2.

Kah, L.C., Lyons, T.W., and Frank, T.D., 2004, Low marine sulphate and protracted oxygenation of the Proterozoic biosphere: Nature, v. 431, p. 834–838, doi:10.1038/nature02974.

Kamber, B.S., and Whitehouse, M.J., 2007, Micro-scale sulphur isotope evidence for sulphur cycling in the late Archean shallow ocean: Geobiology, v. 5, no. 1, p. 5–17.

Kampschulte, A., Bruckschen, P., and Strauss, H., 2001, The sulphur isotopic composition of trace sulphates in Carboniferous brachiopods: Implications for coeval seawater, correlation with other geochemical cycles and isotope stratigraphy: Chemical Geology, v. 175, p. 149–173, doi:10.1016/S0009-2541(00)00367-3.

Kelley, D.S., Delaney, J.R., and Yoerger, D.R., 2001a, Geology and venting characteristics of the Mothra hydrothermal field, Endeavour Segment, Juan de Fuca Ridge: Geology, v. 29, no. 10, p. 959–962, doi:10.1130/0091-7613(2001)029<0959:GAVCOT>2.0.CO;2.

Kelley, D.S., Karson, J.A., Blackman, D.K., Fruh-Green, G.L., Butterfield, D.A., Lilley, M.D., Olson, E.J., Schrenk, M.O., Roe, K.K., Lebon, G.T., Rivizzigno, P., and the AT3-60 Shipboard Party, 2001b, An off-axis hydrothermal vent field near the Mid-Atlantic Ridge at 30°N: Nature, v. 412, no. 6843, p. 145–149, doi:10.1038/35084000.

Kelley, D.S., Karson, J.A., Früh-Green, G.L., Yoerger, D.R., Shank, T.M., Butterfield, D.A., Hayes, J.M., Schrenk, M.O., Olson, E.J., Proskurowski, G., Jakuba, M., Bradley, A., Larson, B., Ludwig, K., Glickson, D., Buckman, K., Bradley, A.S., Brazelton, W.J., Roe, K., Elend, M.J., Delacour, A., Bernasconi, S.M., Lilley, M.D., Baross, J.A., Summons, R.E., and Sylva, S.P., 2005, A serpentinite-hosted ecosystem: The Lost City Hydrothermal Field: Science, v. 307, no. 5714, p. 1428–1434, doi:10.1126/science.1102556.

Kelley, K.D., Leach, D.L., Johnson, C.A., Clark, J.L., Fayek, M., Slack, J.F., Anderson, V.M., Ayuso, R.A., and Ridley, W.I., 2004, Textural, compositional, and sulfur isotope variations of sulfide minerals in the Red Dog Zn-Pb-Ag deposits, Brooks Range, Alaska: Implications for ore formation: Economic Geology and the Bulletin of the Society of Economic Geologists, v. 99, no. 7, p. 1509–1532, doi:10.2113/gsecongeo.99.7.1509.

Koski, R.A., Jonasson, I.R., Kadko, D.C., Smith, V.K., and Wong, F.L., 1994, Compositions, growth mechanisms, and temporal relations of hydrothermal sulfide-sulfate-silica chimneys at the northern Cleft Segment, Juan de Fuca Ridge: Journal of Geophysical Research–Solid Earth, v. 99, no. B3, p. 4813–4832, doi:10.1029/93JB02871.

Kozdon, R., Kita, N.T., Huberty, J.M., Fournelle, J.H., Johnson, C.A., and Valley, J.W., 2010, In situ sulfur isotope analysis of sulfide minerals by SIMS: Precision and accuracy, with application to thermometry of ~3.5Ga Pilbara cherts: Chemical Geology, v. 275, no. 3-4, p. 243–253, doi:10.1016/j.chemgeo.2010.05.015.

Kumar, S., 1995, Megafossils from the Mesoproterozoic Rohtas Formation (the Vindhyan Supergroup), Katni area, central India: Precambrian Research, v. 72, no. 3-4, p. 171–184, doi:10.1016/0301-9268(94)00085-6.

Large, R.R., Bull, S.W., Cooke, D.R., and McGoldrick, P.J., 1998, A genetic model for the H.Y.C. Deposit, Australia; based on regional sedimentology, geochemistry, and sulfide-sediment relationships: Economic Geology and the Bulletin of the Society of Economic Geologists, v. 93, no. 8, p. 1345–1368, doi:10.2113/gsecongeo.93.8.1345.

Large, R.R., Bull, S.W., McGoldrick, P.J., and Walters, S., 2005, Stratiform and strata-bound Zn-Pb-Ag deposits in Proterozoic sedimentary basins, northern Australia: Economic Geology and the Bulletin of the Society of Economic Geologists, v. 100, p. 931–963.

Larter, R.C.L., Boyce, A.J., and Russell, M.J., 1981, Hydrothermal pyrite chimneys from the Ballynoe baryte deposit, Silvermines, County Tipperary, Ireland: Mineralium Deposita, v. 16, no. 2, p. 309–317, doi:10.1007/BF00202742.

Leach, D., Marsh, E., Bradley, D., Gardoll, S., and Huston, D., 2005, The distribution of SEDEX Pb-Zn deposits through Earth history, *in* Mao, J., and Bierlein, F., eds., Mineral Deposit Research: Meeting the Global Challenge: Heidelberg, Springer, p. 145–148.

Leach, D.L., Bradley, D.C., Huston, D., Pisarevsky, S.A., Taylor, R.D., and Gardoll, S.J., 2010, Sediment-hosted lead-zinc deposits in Earth history: Economic Geology and the Bulletin of the Society of Economic Geologists, v. 105, no. 3, p. 593–625, doi:10.2113/gsecongeo.105.3.593.

Lees, J. M., 2014, RFOC: Graphics for Spherical Distributions and Earthquake Focal Mechanisms, R Package Version 3.3-3: Vienna, Austria, R Foundation for Statistical Computing, 156 p.

Li, J., and Kusky, T.M., 2007, World's largest known Precambrian fossil black smoker chimneys and associated microbial vent communities, North China: Implications for early life: Gondwana Research, v. 12, no. 1-2, p. 84–100, doi:10.1016/j.gr.2006.10.024.

Lin, T.J., Ver Eecke, H.C., Breves, E.A., Dyar, M.D., Jamieson, J.W., Hannington, M.D., Dahle, H., Bishop, J.L., Lane, M.D., Butterfield, D.A., Kelley, D.S., Lilley, M.D., Baross, J.A., and Holden, J.F., 2016, Linkages between mineralogy, fluid chemistry, and microbial communities within hydrothermal chimneys from the Endeavour Segment, Juan de Fuca Ridge: Geochemistry Geophysics Geosystems, v. 17, no. 2, p. 300–323, doi:10.1002/2015GC006091.

Little, C.T.S., Herrington, R.J., Maslennikov, V.V., Morris, N.J., and Zaykov, V.V., 1997, Silurian hydrothermal-vent community from the southern Urals, Russia: Nature, v. 385, no. 6612, p. 146–148, doi:10.1038/385146a0.

Little, C.T.S., Herrington, R.J., Maslennikov, V.V., and Zaykov, V.V., 1998, The fossil record of hydrothermal vent communities, *in* Mills, R.A., and Harrison, K., eds., Modern Ocean Floor Processes and the Geological Record: Geological Society, London, Special Publication 148, p. 259–270, doi:10.1144/GSL.SP.1998.148.01.14.

Little, C.T.S., Cann, J.R., Herrington, R.J., and Morisseau, M., 1999a, Late Cretaceous hydrothermal vent communities from the Troodos ophiolite, Cyprus: Geology, v. 27, no. 11, p. 1027–1030, doi:10.1130/0091-7613(1999)027<1027:LCHVCF>2.3.CO;2.

Little, C.T.S., Herrington, R.J., Haymon, R.M., and Danelian, T., 1999b, Early Jurassic hydrothermal vent community from the Franciscan complex, San Rafael Mountains, California: Geology, v. 27, no. 2, p. 167–170, doi:10.1130/0091-7613(1999)027<0167:EJHVCF>2.3.CO;2.

Love, L.G., 1971, Early diagenetic polyframboidal pyrite, primary and redeposited, from the Wenlockian Denbigh Grit Group, Conway, North Wales, U.K.: Journal of Sedimentary Research, v. 41, no. 4, p. 1038–1044.

Ludwig, K.A., Kelley, D.S., Butterfield, D.A., Nelson, B.K., and Früh-Green, G., 2006, Formation and evolution of carbonate chimneys at the Lost City Hydrothermal Field: Geochimica et Cosmochimica Acta, v. 70, no. 14, p. 3625–3645, doi:10.1016/j.gca.2006.04.016.

Luepke, J.J., and Lyons, T.W., 2001, Pre-Rodinian (Mesoproterozoic) supercontinental rifting along the western margin of Laurentia: Geochemical evidence from the Belt-Purcell Supergroup: Precambrian Research, v. 111, no. 1-4, p. 79–90, doi:10.1016/S0301-9268(01)00157-7.

Luo, G., Ono, S., Huang, J., Algeo, T.J., Li, C., Zhou, L., Robinson, A., Lyons, T.W., and Xie, S., 2015, Decline in oceanic sulfate levels during the early Mesoproterozoic: Precambrian Research, v. 258, p. 36–47, doi:10.1016/j.precamres.2014.12.014.

Lydon, J.W., 1996, Sedimentary exhalative sulphides (SEDEX), *in* Eckstrand, O.R., Sinclair, W.D., and Thorpe, R.I., eds., Geology of Canadian Mineral Deposit Types: Geological Survey of Canada, Geology of Canada 8, p. 130–152.

Lyons, T.W., Frank, T.D., Schreiber, M.E., Winston, D., and Lohmann, K.C., 1993, Geochemical constraints on paleoenvironments within the Belt Supergroup (Middle Proterozoic), Montana, *in* Berg, R.B., ed., Belt Symposium III: Montana Bureau of Mines and Geology Special Publication 112, p. 190–201.

Lyons, T.W., Luepke, J.J., Schreiber, M.E., and Zieg, G.A., 2000, Sulfur geochemical constraints on Mesoproterozoic restricted marine deposition: Lower Belt Supergroup, northwestern United States: Geochimica et Cosmochimica Acta, v. 64, no. 3, p. 427–437, doi:10.1016/S0016-7037(99)00323-3.

Lyons, T.W., Walter, L.M., Gellatly, A.M., Martini, A.M., and Blake, R.E., 2004, Sites of anomalous organic remineralization in the carbonate sediments of south Florida, USA: The sulfur cycle and carbonate-associated sulfate, *in* Amend, J.P., Edwards, K.J., and Lyons, T.W., eds., Sulfur Biogeochemistry—Past and Present: Geological Society of America Special Paper 379, p. 161–176.

Lyons, T.W., Gellatly, A.M., McGoldrick, P.J., and Kah, L.C., 2006, Proterozoic sedimentary exhalative (SEDEX) deposits and links to evolving global ocean chemistry, *in* Kesler, S.E., and Ohmoto, H., eds., Evolution of Early Earth's Atmosphere, Hydrosphere, and Biosphere—Constraints from Ore Deposits: Geological Society of America Memoir 198, p. 169–184.

Marin-Carbonne, J., Rollion-Bard, C., Bekker, A., Rouxel, O., Agangi, A., Cavalazzi, B., Wohlgemuth-Ueberwasser, C.C., Hofmann, A., and McKeegan, K.D., 2014, Coupled Fe and S isotope variations in pyrite nodules from Archean

shale: Earth and Planetary Science Letters, v. 392, p. 67–79, doi:10.1016/j.epsl.2014.02.009.

McGoldrick, P., 1998, Halo model for the Grevillea Prospect, *in* Leaman, D., Bull, S., Winefield, P., Selley, D., Scott, R., Cooke, D., McGoldrick, P., Large, R., and Garven, G., eds., Sediment-Hosted Base Metal Deposits: Project Outcomes Report, AMIRA/ARC Project P384A: Tasmania, Center for Ore Deposit Research (CODES SRC), University of Tasmania Hobart, p. 157–167.

McGoldrick, P., 1999, Northern Australian Sedex deposits: Microbial oases in Proterozoic seas, *in* Stanley, C., ed., Proceedings of the Fifth Biennial SGA Meeting and Tenth Quadrennial International Association on the Genesis of Ore Deposits Symposium: Rotterdam, CRC Press, p. 885–888.

McGoldrick, P., and Zieg, J., Massive microbes from the Mesoproterozoic of Montana?: Proceedings of the Geological Society of Australia Abstracts 2004, v. 73, p. 100.

Moore, D.W., Young, L.E., Modene, J.S., and Plahuta, J.T., 1986, Geologic setting and genesis of the Red Dog zinc-lead-silver deposit, western Brooks Range, Alaska: Economic Geology and the Bulletin of the Society of Economic Geologists, v. 81, no. 7, p. 1696–1727, doi:10.2113/gsecongeo.81.7.1696.

Murowchick, J.B., and Barnes, H.L., 1986, Marcasite precipitation from hydrothermal solutions: Geochimica et Cosmochimica Acta, v. 50, no. 12, p. 2615–2629, doi:10.1016/0016-7037(86)90214-0.

Oehler, J.H., and Logan, R.G., 1977, Microfossils, cherts, and associated mineralization in the Proterozoic McArthur (H.Y.C.) lead-zinc-silver deposit: Economic Geology and the Bulletin of the Society of Economic Geologists, v. 72, no. 8, p. 1393–1409, doi:10.2113/gsecongeo.72.8.1393.

Okumura, T., Ohara, Y., Stern, R., Yamanaka, T., Onishi, Y., Watanabe, H., Chen, C., Bloomer, S., Pujana, I., and Sakai, S., 2016, Brucite chimney formation and carbonate alteration at the Shinkai Seep Field, a serpentinite-hosted vent system in the southern Mariana forearc: Geochemistry, Geophysics, Geosystems, v. 17, no. 9, p. 3775–3796, doi:10.1002/2016GC006449.

Paris, G., Sessions, A.L., Subhas, A.V., and Adkins, J.F., 2013, MC-ICP-MS measurement of $\delta^{34}S$ and $\Delta^{33}S$ in small amounts of dissolved sulfate: Chemical Geology, v. 345, p. 50–61, doi:10.1016/j.chemgeo.2013.02.022.

Paris, G., Adkins, J.F., Sessions, A.L., Webb, S.M., and Fischer, W.W., 2014, Neoarchean carbonate-associated sulfate records positive $\Delta^{33}S$ anomalies: Science, v. 346, no. 6210, p. 739–741, doi:10.1126/science.1258211.

Planavsky, N.J., McGoldrick, P., Scott, C.T., Li, C., Reinhard, C.T., Kelly, A.E., Chu, X., Bekker, A., Love, G.D., and Lyons, T.W., 2011, Widespread iron-rich conditions in the mid-Proterozoic ocean: Nature, v. 477, no. 7365, p. 448–451, doi:10.1038/nature10327.

Powell, T.G., and Macqueen, R.W., 1984, Precipitation of sulfide ores and organic matter: Sulfate reactions at Pine Point, Canada: Science, v. 224, no. 4644, p. 63–66, doi:10.1126/science.224.4644.63.

Present, T.M., Paris, G., Burke, A., Fischer, W.W., and Adkins, J.F., 2015, Large carbonate associated sulfate isotopic variability between brachiopods, micrite, and other sedimentary components in Late Ordovician strata: Earth and Planetary Science Letters, v. 432, p. 187–198, doi:10.1016/j.epsl.2015.10.005.

R Core Team, 2015, R: A Language and Environment for Statistical Computing: Vienna, Austria, R Foundation for Statistical Computing.

Reitner, J., Peckmann, J., Reimer, A., Schumann, G., and Thiel, V., 2005, Methane-derived carbonate build-ups and associated microbial communities at cold seeps on the lower Crimean shelf (Black Sea): Facies, v. 51, no. 1-4, p. 66–79, doi:10.1007/s10347-005-0059-4.

Rennie, V.C.F., and Turchyn, A.V., 2014, The preservation of and in carbonate-associated sulfate during marine diagenesis: A 25 Myr test case using marine sediments: Earth and Planetary Science Letters, v. 395, p. 13–23, doi:10.1016/j.epsl.2014.03.025.

Rohrlach, B.D., Fu, M., and Clarke, J.D.A., 1998, Geological setting, paragenesis and fluid history of the Walford Creek Zn-Pb-Cu-Ag prospect, Mt. Isa Basin, Australia: Australian Journal of Earth Sciences, v. 45, no. 1, p. 63–81, doi:10.1080/08120099808728367.

Russell, M.J., and Hall, A., 1997, The emergence of life from iron monosulphide bubbles at a submarine hydrothermal redox and pH front: Journal of the Geological Society [London], v. 154, no. 3, p. 377–402, doi:10.1144/gsjgs.154.3.0377.

Russell, M.J., Solomon, M., and Walshe, J., 1981, The genesis of sediment-hosted, exhalative zinc+lead deposits: Mineralium Deposita, v. 16, no. 1, p. 113–127, doi:10.1007/BF00206458.

Russell, M.J., Hall, A.J., and Turner, D., 1989, In vitro growth of iron sulphide chimneys: Possible culture chambers for origin-of-life experiments: Terra Nova, v. 1, no. 3, p. 238–241, doi:10.1111/j.1365-3121.1989.tb00364.x.

Samson, I.M., and Russell, M.J., 1987, Genesis of the Silvermines zinc-lead-barite deposit, Ireland; fluid inclusion and stable isotope evidence: Economic Geology and the Bulletin of the Society of Economic Geologists, v. 82, no. 2, p. 371–394, doi:10.2113/gsecongeo.82.2.371.

Sangster, D.F., 2002, The role of dense brines in the formation of vent-distal sedimentary-exhalative (SEDEX) lead-zinc deposits: Field and laboratory evidence: Mineralium Deposita, v. 37, no. 2, p. 149–157, doi:10.1007/s00126-001-0216-9.

Schieber, J., 1989a, Facies and origin of shales from the mid-Proterozoic Newland Formation, Belt Basin, Montana, USA: Sedimentology, v. 36, no. 2, p. 203–219, doi:10.1111/j.1365-3091.1989.tb00603.x.

Schieber, J., 1989b, The origin of the Neihart Quartzite, a basal deposit of the mid-Proterozoic Belt Supergroup, Montana, USA: Geological Magazine, v. 126, no. 3, p. 271–281, doi:10.1017/S0016756800022366.

Schieber, J., 1989c, Pyrite mineralization in microbial mats from the mid-Proterozoic Newland Formation, Belt Supergroup, Montana, USA: Sedimentary Geology, v. 64, no. 1-3, p. 79–90, doi:10.1016/0037-0738(89)90085-7.

Schieber, J., 1990, Pyritic shales and microbial mats: Significant factors in the genesis of stratiform Pb-Zn deposits of the Proterozoic?: Mineralium Deposita, v. 25, no. 1, p. 7–14, doi:10.1007/BF03326378.

Schieber, J., 2011, Marcasite in black shales—A mineral proxy for oxygenated bottom waters and intermittent oxidation of carbonaceous muds: Journal of Sedimentary Research, v. 81, no. 7, p. 447–458, doi:10.2110/jsr.2011.41.

Schoonen, M.A.A., and Barnes, H.L., 1991, Reactions forming pyrite and marcasite from solution: II. Via FeS precursors below 100°C: Geochimica et Cosmochimica Acta, v. 55, no. 6, p. 1505–1514, doi:10.1016/0016-7037(91)90123-M.

Schrenk, M.O., Kelley, D.S., Bolton, S.A., and Baross, J.A., 2004, Low archaeal diversity linked to subseafloor geochemical processes at the Lost City Hydrothermal Field, Mid-Atlantic Ridge: Environmental Microbiology, v. 6, no. 10, p. 1086–1095, doi:10.1111/j.1462-2920.2004.00650.x.

Sears, J.W., Chamberlain, K.R., and Buckley, S.N., 1998, Structural and U-Pb geochronological evidence for 1.47 Ga rifting in the Belt Basin, western Montana: Canadian Journal of Earth Sciences, v. 35, no. 4, p. 467–475, doi:10.1139/e97-121.

Shapiro, R., and Fricke, H., 2002, Tepee Buttes: Fossilized methane-seep ecosystems: Field Guides, v. 3, p. 94–101.

Slotznick, S.P., Zieg, J., Webb, S.M., Kirschvink, J.L., and Fischer, W.W., 2015, Iron mineralogy and redox chemistry of the Mesoproterozoic Newland Formation in the Helena Embayment, Belt Supergroup, Montana: Northwest Geology, v. 44, p. 55–72.

Sperling, E.A., Rooney, A.D., Hays, L., Sergeev, V., Vorob'eva, N., Sergeeva, N., Selby, D., Johnston, D.T., and Knoll, A.H., 2014, Redox heterogeneity of subsurface waters in the Mesoproterozoic ocean: Geobiology, v. 12, no. 5, p. 373–386, doi:10.1111/gbi.12091.

Steen, I.H., Dahle, H., Stokke, R., Roalkvam, I., Daae, F.-L., Rapp, H.T., Pedersen, R.B., and Thorseth, I.H., 2016, Novel barite chimneys at the Loki's Castle Vent Field shed light on key factors shaping microbial communities and functions in hydrothermal systems: Frontiers in Microbiology, v. 6, no. 1510, p. 1–13.

Strauss, H., 1993, The sulfur isotopic record of Precambrian sulfates: New data and a critical evaluation of the existing record: Precambrian Research, v. 63, p. 225–246, doi:10.1016/0301-9268(93)90035-Z.

Strauss, H., and Schieber, J., 1990, A sulfur isotope study of pyrite genesis—The Mid-Proterozoic Newland Formation, Belt Supergroup, Montana: Geochimica et Cosmochimica Acta, v. 54, no. 1, p. 197–204, doi:10.1016/0016-7037(90)90207-2.

Tivey, M.K., 1995, Modeling chimney growth and associated fluid flow at seafloor hydrothermal vent sites, *in* Humphris, S.E., Zierenberg, R.A., Mullineaux, L.S., and Thomson, R.E., eds., Seafloor Hydrothermal Systems: Physical, Chemical, Biological, and Geological Interactions: American Geophysical Union Geophysical Monograph 91, p. 158–177.

Tivey, M.K., 2007, Generation of seafloor hydrothermal vent fluids and associated mineral deposits: Oceanography (Washington, D.C.), v. 20, no. 1, p. 50–65, doi:10.5670/oceanog.2007.80.

Torres, M.E., Brumsack, H.J., Bohrmann, G., and Emeis, K.C., 1996, Barite fronts in continental margin sediments: A new look at barium remobilization in the zone of sulfate reduction and formation of heavy barites in diagenetic fronts: Chemical Geology, v. 127, p. 125–139, doi:10.1016/0009-2541(95)00090-9.

Walter, M., Du, R., and Horodyski, R.J., 1990, Coiled carbonaceous megafossils from the Middle Proterozoic of Jixian (Tianjin) and Montana: American Journal of Science, v. 290-A, p. 133–148.

White, J., Gammons, C.H., and Zieg, G.A., 2013, Paragenesis of cobalt and nickel in the Black Butte shale-hosted copper deposit, Belt Basin, Montana, USA: Mineralium Deposita, v. 49, p. 335–351, doi:10.1007/s00126-013-0492-1.

Winston, D., and Link, P., 1993, Middle Proterozoic rocks of Montana, Idaho and eastern Washington: The Belt Supergroup, *in* Reed, J.C., Jr., Bickford, M.E., Houston, R.S., Link, P.K., Rankin, R.W., Sims, P.K., and Van Schmus, W.R., eds., Precambrian: Conterminous U.S.: Boulder, Colorado, Geological Society of America, The Geology of North America, v. C-2, p. 487–517.

Xiao, Z., Gammons, C.H., and Williams-Jones, A.E., 1998, Experimental study of copper(I) chloride complexing in hydrothermal solutions at 40 to 300°C and saturated water vapor pressure: Geochimica et Cosmochimica Acta, v. 62, no. 17, p. 2949–2964, doi:10.1016/S0016-7037(98)00228-2.

Zieg, G.A., 1986, Stratigraphy and sedimentology of the Middle Proterozoic upper Newland Limestone, *in* Roberts, S.M., ed., Belt Supergroup: A Guide to the Proterozoic Rocks of Western Montana and Adjacent Areas: Montana Bureau of Mines and Geology Special Publication 94, p. 125–141.

Zieg, G.A., and Leitch, C.H., 1998, The geology of the Sheep Creek copper deposit, Meagher County, Montana, *in* Berg, R., ed., Belt Symposium III Abstracts: Montana Bureau of Mines and Geology (MBMG) Open-File Report 381, p. 67–69.

Zieg, G.A., Scartozzi, V., Chutas, N., Albers, D., Gostomski, K., and Jones, J., 2013, Black Butte Copper deposits, Lower Belt Supergroup, Montana: Northwest Geology, v. 42, p. 131–148.

Science Editor: Aaron J. Cavosie
Associate Editor: Fernando Corfu

Manuscript Received 31 January 2016
Revised Manuscript Received 27 April 2017
Manuscript Accepted 12 July 2017

Printed in the USA